Petroleum Science
https://doi.org/10.1007/s12182-020-00434-0

ORIGINAL PAPER

The nature, type, and origin of diagenetic fluids and their control on the evolving porosity of the Lower Cambrian Xiaoerbulak Formation dolostone, northwestern Tarim Basin, China

Pei-Xian Liu[1] · Shi-Biao Deng[1] · Ping Guan[1] · Yi-Qiu Jin[2] · Kai Wang[1] · Yong-Quan Chen[3]

Received: 16 March 2019

Abstract
The study on Lower Cambrian dolostones in Tarim Basin can improve our understanding of ancient and deeply buried carbonate reservoirs. In this research, diagenetic fluid characteristics and their control on porosity evolution have been revealed by studying the petrography and in situ geochemistry of different dolomites. Three types of diagenetic fluids were identified: (1) Replacive dolomites were deviated from shallow burial dolomitizing fluids, which might probably be concentrated ancient seawater at early stage. (2) Fine-to-medium crystalline, planar-e diamond pore-filling dolomites (Fd1) were likely slowly and sufficiently crystallized from deep-circulating crustal hydrothermal fluids during Devonian. (3) Coarse crystalline, non-planar-a saddle pore-filling dolomites (Fd2) might rapidly and insufficiently crystallize from magmatic hydrothermal fluids during Permian. Early dolomitizing fluids did not increase the porosity, but transformed the primary pores to dissolution pores through dolomitization. Deep-circulating crustal hydrothermal fluids significantly increased porosity in the early stages by dissolving and then slightly decreased the porosity in the late stage due to Fd1 precipitation. Magmatic hydrothermal fluids only precipitated the Fd2 dolomites and slightly decreased the porosity. In summary, Devonian deep-circulating crustal hydrothermal fluids dominated the porosity evolution of the Lower Cambrian dolostone reservoir in the Tarim Basin.

Keywords Lower Cambrian · Dolostone reservoir · In situ geochemistry · Diagenetic fluids · Porosity evolution

1 Introduction

Dolostone reservoirs are important components of carbonate hydrocarbon reservoirs in many petroliferous basins worldwide (Ehrenberg et al. 2006; Li et al. 2011a, b; Sonnenberg and Pramudito 2009; Sun 1995; Warren 2000; Zhao et al. 2005), but dolomite genesis and the mechanism for generating dolostone reservoirs remain intensely debated (Hardie 1987; Kirmaci and Akdag 2005; Machel 2004; Morrow 1998; Warren 2000; You et al. 2015). Recent geophysical research found the Lower Cambrian platform margin facies dolostones in the subsurface of the Tabei Uplift (Ni et al. 2015), which made the Lower Cambrian Xiaoerbulak Formation dolostones become potential exploration targets for hydrocarbon reservoirs (Du and Pan 2016; Liu et al. 2017). Limited by scarce well samples, researches on the Lower Cambrian dolostones were mainly conducted in the Sugetbulak outcrop area of the northwestern Tarim Basin, where abundant pores, bitumen, and plentiful pore-filling dolomites were found (Li et al. 2011a, b, 2015; Song et al. 2014). Recent researches show that high-quality reservoirs in the Xiaoerbulak Formation are mainly distributed in the platform margin facies dolograinstones (Li et al. 2015; Song et al. 2014) and a few microbial dolostones (Li et al. 2015; Song et al. 2014).

The Lower Cambrian dolostone reservoirs are regarded as one of the most ancient and deeply buried carbonate reservoirs in the world (Li et al. 2016; Pan et al. 2012; Zhang et al. 2014). However, the formation mechanism of the

Edited by Jie Hao

✉ Ping Guan
pguanl@pku.edu.cn

[1] Key Laboratory of Orogenic Belts and Crustal Evolution, School of Earth and Space Sciences, Peking University, Beijing 100871, China

[2] Research Institute of Petroleum Exploration and Development, PetroChina, Beijing 100083, China

[3] Research Institute of Petroleum Exploration and Development, Tarim Oilfield Branch, PetroChina, Korla 841000, Xinjiang, China

Published online: 06 June 2020

high-quality dolostone reservoirs remains unknown. Due to the lack of systematically petrographic and geochemical studies, the origin and nature of different diagenetic fluids remain debated. Previous studies concluded that the genesis of the Lower Cambrian dolostones was controlled by one or a mixture of three types of diagenetic fluids: meteoric water, concentrated seawater or heated formation water, and hydrothermal fluids (Cai et al. 2008; Ji et al. 2013; Li et al. 2011a, b; Pan et al. 2012; Zhang et al. 2011, 2014; Zhu et al. 2010). However, the correlation between different types of dolomites and their forming fluids remain unclear, as well as the origin and nature of these different diagenetic fluids (Zhang et al. 2014). Some studies concluded that the saddle dolomite and recrystallized dolomites were precipitated from magmatic hydrothermal fluid (Chen et al. 2009a; Dong et al. 2013; Pan et al. 2009; Zhao et al. 2012; Zhu et al. 2010). Other studies proposed that these dolomites were precipitated from stratigraphic hydrothermal fluids (Pan et al. 2012), such as the heated formation water from the Cambrian dolomite strata (Qian et al. 2012; Zhang et al. 2009, 2011).

Moreover, the influence of the diagenetic fluids on the formation of such a reservoir is also unclear. For example, previous studies (Li et al. 2011a, b; Li et ai. 2016) concluded that primary pores were strongly cemented, and the high-quality dolostone reservoirs were mainly resulted from the corrosion of deep hydrothermal fluids based on the geochemistry property of pore-filling dolomites. However, recent studies have also identified abundant interparticle and intercrystalline pores without any pore-filling dolomites, thus concluding that the primary pores were only slightly cemented and further dissolution occurred during epidiagenesis (Li et al. 2015; Shen et al. 2016).

Based on the basin's sedimentary, tectonic evolution and systematically petrographic and in situ geochemical research on different types of dolomites and reservoir spaces in the dolostones of the Lower Cambrian Xiaoerbulak Formation, this study (1) identified the types, nature, and origin of diagenetic fluids for different dolomites; (2) clarified the influence of different diagenetic fluids on the formation of reservoir spaces; and (3) explained the porosity evolution of the high-quality dolostone reservoir controlled by multiple-stage diagenetic fluids. The results of this study can improve our understanding of very ancient and deeply buried carbonate reservoirs.

2 Geological setting

The Tarim Basin is the largest basin in China with an area of nearly 560,000 km^2 (Wang et al. 2009). The basin is located in northwestern China (Fig. 1a), surrounded by the Tian Shan Mountains and West Kunlun–Altun Mountains in the north and south, respectively (Fig. 1b). The basin has undergone a multiple-stage history of tectonic evolutionary processes, e.g., the Caledonian, Hercynian, Indosinian, and Himalayan cycles (Tang 1997). The six evolution stages during the Phanerozoic can be generally divided into the (1) intra-cratonic extensional basin stage during the Sinian–Early Ordovician, (2) intra-cratonic compressional basin stage during the Middle Ordovician–Middle Devonian, (3) back-arc extensional basin stage during the Late Devonian–Early Permian, (4) retro-arc foreland basin stage during the Late Permian–Triassic, (5) collisional reactivated foreland basin stage during the Jurassic–Paleogene, and (6) Indian–Tibetan collisional successor basin stage during the Neogene–Quaternary (Li 1995; Li et al. 2016; Zhang et al. 2009). Now, the basin is roughly divided into nine principal structural units, including four major uplifts, the Tabei, Tazhong, Bachu, and Southeast, and five major depressions (Fig. 1b), the Kuche, North, Tanggu, Southwest, and Southeast (Wang et al. 1992; Zhang et al. 2014). As a giant petroliferous basin, it contains abundant petroleum and natural gas resources, and the verified hydrocarbon reservoirs include Cambrian and Ordovician marine carbonate reservoirs, Silurian to Carboniferous marine clastic reservoirs, Permian volcanic reservoirs, and Mesozoic and Cenozoic terrestrial fluvial clastic reservoirs (Gu et al. 2002; Pu et al. 2011).

Sedimentation in the western Tarim Basin consists of Neoproterozoic beach to shallow marine facies siliciclastic rocks and carbonates, followed by Cambrian and Ordovician platform facies limestones and dolostones, and slope facies limestones and marls. Silurian, Ordovician, and Carboniferous strata consist of marine siliciclastic rocks (Cai et al. 2001a, 2001b, 2008; Li et al. 2011a, b; Zhang et al. 2014). Permian sequences are mainly composed of lacustrine sediments and widely distributed volcanic rocks, including basalt, rhyolite, diabase intrusions, and granite intrusions (Zhang et al. 2008; Tian et al. 2010; Zhang et al. 2010, 2014). Mesozoic and Cenozoic sequences are mainly terrestrial fluvial sandstones and mudstones (Cai et al. 2001a, b, 2008; Li et al. 2011a, b; Zhang et al. 2014).

Dolostones are indispensable components of marine carbonate reservoirs in the Tarim Basin (Zheng et al. 2007). Dolostone strata of the basin mainly developed from the Upper Sinian Qigbulak Formation to Lower Ordovician Penglaiba Formation. These dolostones are divided into post-salt and pre-salt petroliferous sequences by regionally distributed Middle Cambrian evaporites interlaying between them (Fig. 2). Numerous wells have been drilled in the post-salt sequences, and Upper Cambrian–Lower Ordovician dolostone reservoirs have been proven excellent (Chen et al. 2009b; Huang et al. 2012). However, the pre-salt sequence is buried underground to depths of 6000–8000 m in the uplifts and 8000–12,000 m in the depressions, overlain

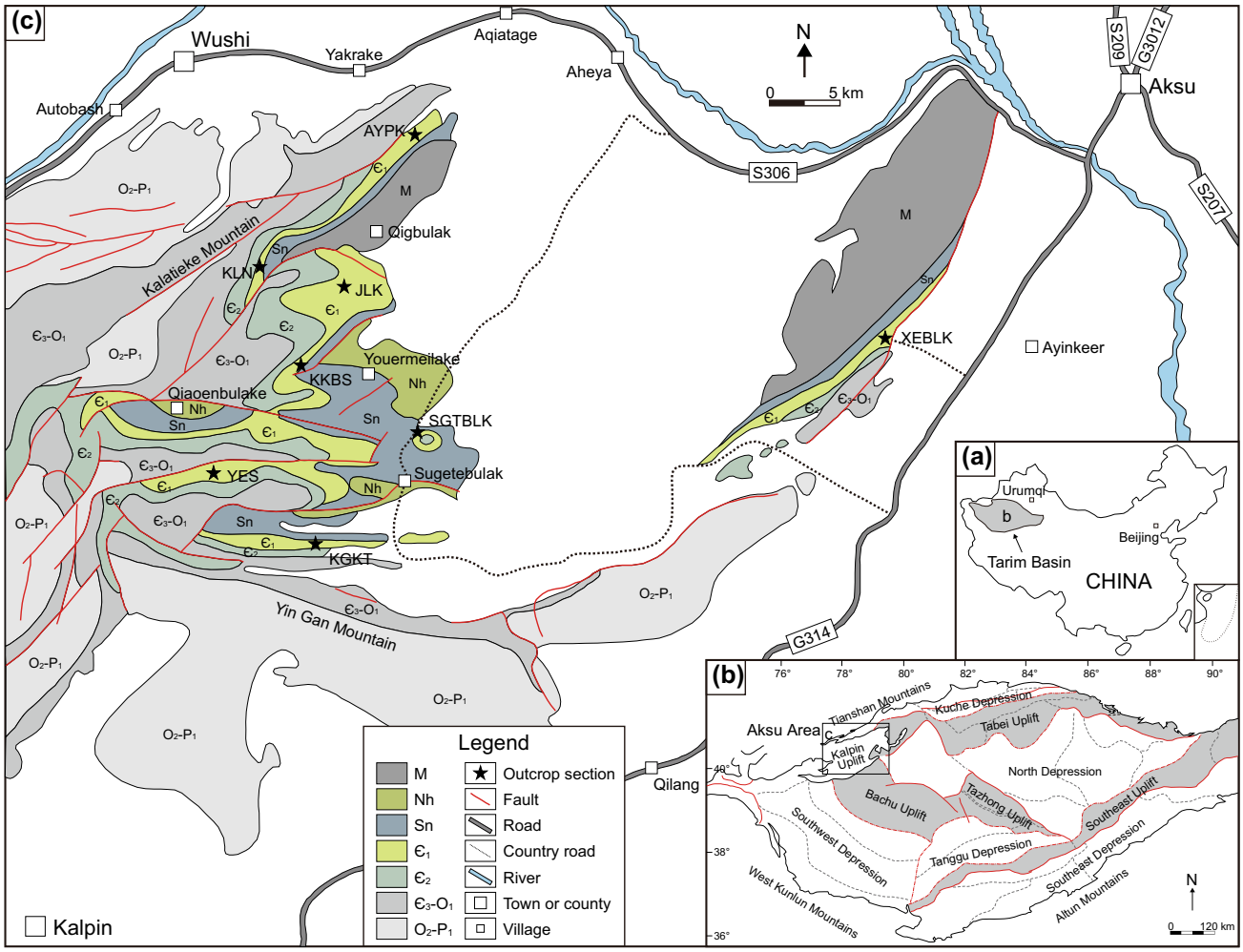

Fig. 1 **a** Location of the Tarim Basin in northwestern China. **b** Tectonic location of the study area indicated with a black rectangle. **c** Geological setting of the northwestern Tarim Basin and outcrop section locations for sampling. Stratigraphic system: M, Mesoproterozoic metamorphic basement of Aksu Group; Nh, Neoproterozoic Nanhua system; Sn, Neoproterozoic Sinian system; Є, Cambrian; O, Ordovician; P, Permian. Section names are all based on the nearby villages: AYPK, Aoyipike; KLN, Kulunan; JLK, Jinlinkuang; KKBS, Kakebashi; SGTBLK, Sugaitebulake; YES, Yingersu; KGKT, Konggaikuotan; XEBLK, Xiaoerbulak

by thick Middle Cambrian evaporites (Zhu et al. 2014). As a result, only a few deep wells have been drilled into Lower Cambrian stratum and core samples are rare. Hence, observational and geochemical studies of the Lower Cambrian dolostones are primarily conducted at field sites.

This study was conducted in the Aksu Area of the northwestern Tarim Basin (Fig. 1c), where the Lower Cambrian sequences are well exposed (Fig. 3a). The area lies within the Kalpin Uplift Unit, where a series of folds and thrust belts trend northeast due to the compressional orogeny of the southern Tian Shan Mountains in late Cenozoic (Burchfiel et al. 1999; Li et al. 2015, 2016). As a result, the Lower Cambrian stratum is segmented and distributed in several thrust fold belts (Fig. 1c). Preliminary research of the Lower Cambrian dolostones in this area was performed on eight field outcrop sections by our group (Li et al. 2015), which correlated stratigraphy, classified sedimentary facies, measured porosity, and evaluated the reservoirs (Fig. 1c). The Xiaoerbulak Formation is considered the main reservoir interval of the Lower Cambrian (Li et al. 2015; Shen et al. 2016) because of the intensely developed pores (Fig. 3b, c). From the bottom upward, this formation is composed of platform margin facies micritic–microspar dolostones (Fig. 3d), agglutinated microbial reef dolostones (Fig. 3e), dolograinstone (Fig. 3f), and laminated microbial dolostones (Fig. 3g) (Li et al. 2015). Dolograinstone is the dominant high-quality reservoir due to its high average porosity (7%–8%) and the large-scale distribution surrounding the Lower Cambrian platform margin, with thicknesses of ~ 40 m and width of approximately 25 km (Li et al. 2015).

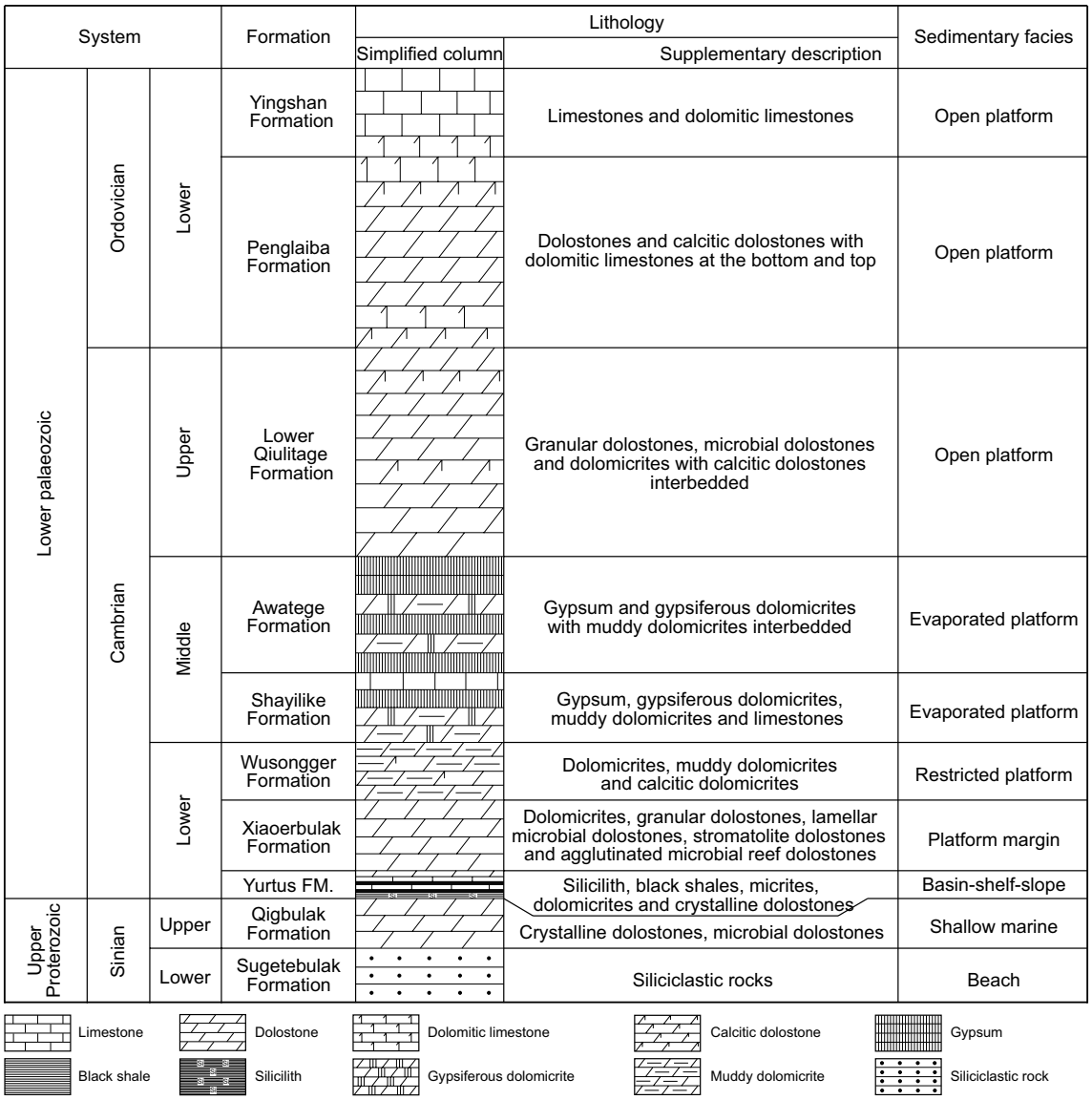

Fig. 2 Sinian-Lower Ordovician stratigraphic framework, lithological description, and sedimentary facies of the northwestern Tarim Basin

3 Methods

A total of 267 dolostone samples were collected from eight outcrop sections (Fig. 1c), covering all lithofacies described in Sect. 2. Sampling points and serial numbers were marked on corresponding lithological columns (Fig. 4). Thin sections were separately cut from all samples to study the petrographic and reservoir porosity. Dilute hydrochloric acid and alizarin red-S were used to examine the mineralogy in hand specimen and thin sections (Friedman 1959). The scheme of Gregg and Sibley (1984) and Sibley and Gregg (1987) was adopted for the petrographic descriptions and classifications. Descriptions of the reservoir porosity used the classification system of Choquette and Pray (1970). Thirteen representative samples, marked with black stars in Fig. 4, were selected for in situ geochemical experiments.

Three types of replacive dolomites (Rd) and two types of pore-filling dolomites (Fd) are classified based on petrography. Due to the sedimentary textures and heterogeneous recrystallization of the samples, three types of replacive dolomites (Rds) commonly have intergrowth relationships. However, their crystals are too small to separate at macroscopic scale and can only be distinguished under microscope. Two types of pore-filling dolomites (Fds) usually develop in pores and small fractures, and they often have an intergrowth relationship (Fig. 5a–d), which is occasionally accompanied by late-stage filling calcites (Fig. 5b). Hence, although these pore-filling dolomites can be distinguished at the macroscopic scale, it is challenging to separate them

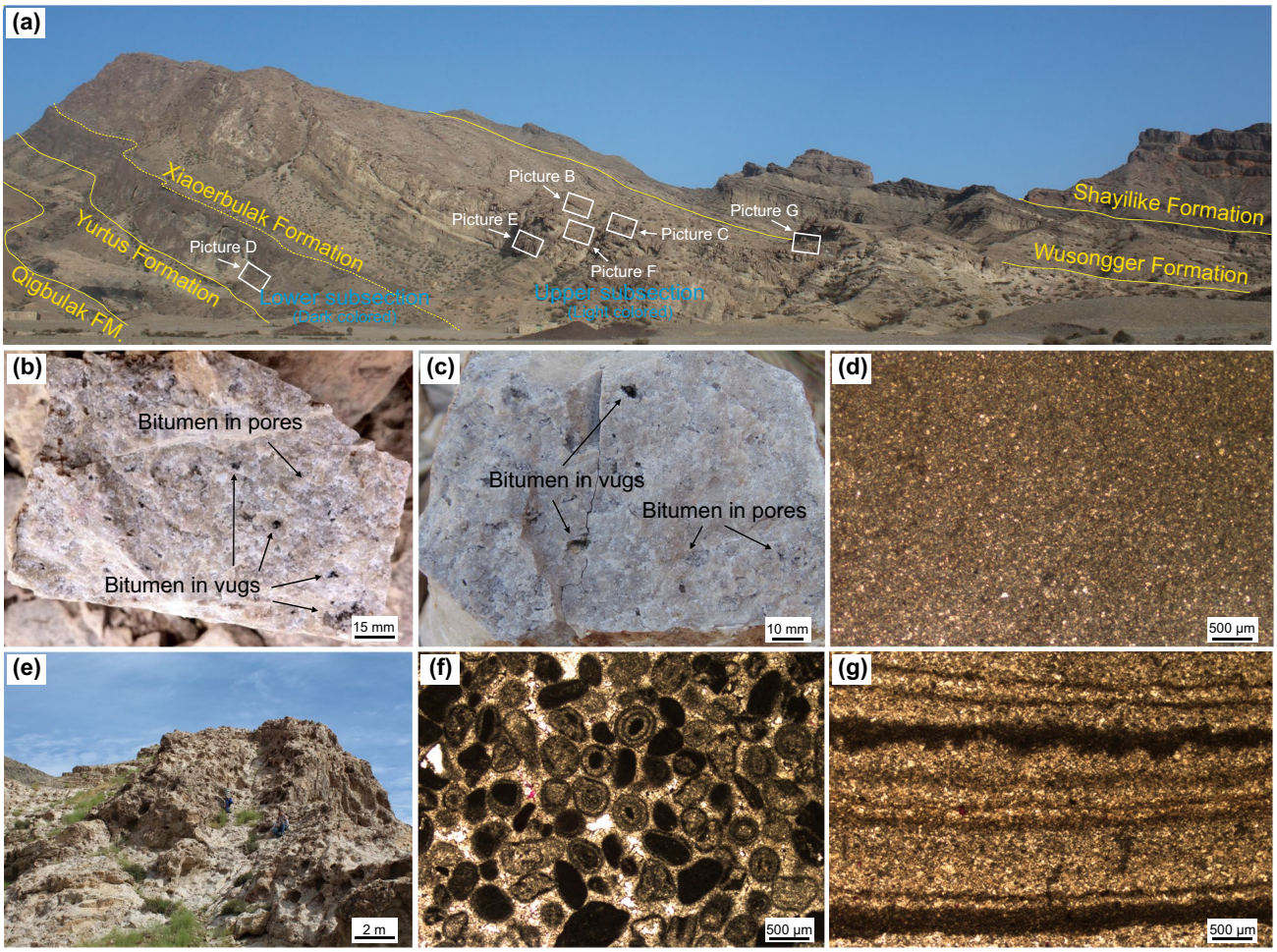

Fig. 3 **a** Stratigraphy of the Upper Sinian–Middle Cambrian in the SGT section and the distributions of different dolostone lithofacies of the Xiaoerbulak Formation in pictures B–G. **b**, **c** Dolograinstone with plentiful pores and bitumen. **d** Dark gray micritic dolostone. **e** Agglutinated microbial reef dolostones. **f** Dolograinstone. **g** Laminated microbial dolostones

with microdrilling due to their mixing and the disturbance of replacive dolomites and filling calcites. Therefore, to avoid mixing between the different generations, the in situ LA-ICP-MS method was adopted in this study.

A total of 66 test spots were designed to measure the in situ trace and rare-earth elemental composition of different types of dolomites. The tests were accomplished at the Key Laboratory of Orogenic Belts and Crustal Evolution, Peking University, using Laser Ablation Inductively Coupled Plasma Mass Spectrometry (LA-ICP-MS). In situ LA-ICP-MS analysis has been widely used on carbonates due to its high sensitivity, excellent spatial resolution (Kamber and Webb 2007; Jochum et al. 2012; Lazartigues et al. 2014; Zhang et al. 2014), and reliable methodology (Chen et al. 2011; Lazartigues et al. 2014). An Agilent 7500ce ICP-MS equipped with a COMPEX Pro 102 laser ablation system with a 193 nm ArF-excimer laser (Li et al. 2013) using helium as the carrier gas to increase ablated sample transport efficiency was used. The size of the laser-circular spot remained constant at 60 μm in diameter. Carbonate reference materials NIST 610 and 612 were tested as external standards to monitor analytical precision and accuracy. The accuracy was estimated to be $<0.6\%$ for all trace and rare-earth elements in NIST 610 and $<5\%$ in NIST 612 (Gao et al. 2002). The detection limits (i.e., background level) varied from 0.003 to 0.30 ppm for most elements except Mn (1.00 ppm), Fe (6.10 ppm), Zn (1.50 ppn), and Ba (0.40 ppm) in this study due to the influence of equipment conditions (Lazartigues et al. 2014).

4 Petrography

Three kinds of replacive dolomites (Rd), two kinds of pore-filling dolomites (Fd), and one kind of pore-filling calcite (Fc) were recognized by petrography. What is more, five types of reservoir space and their filling situation were summarized.

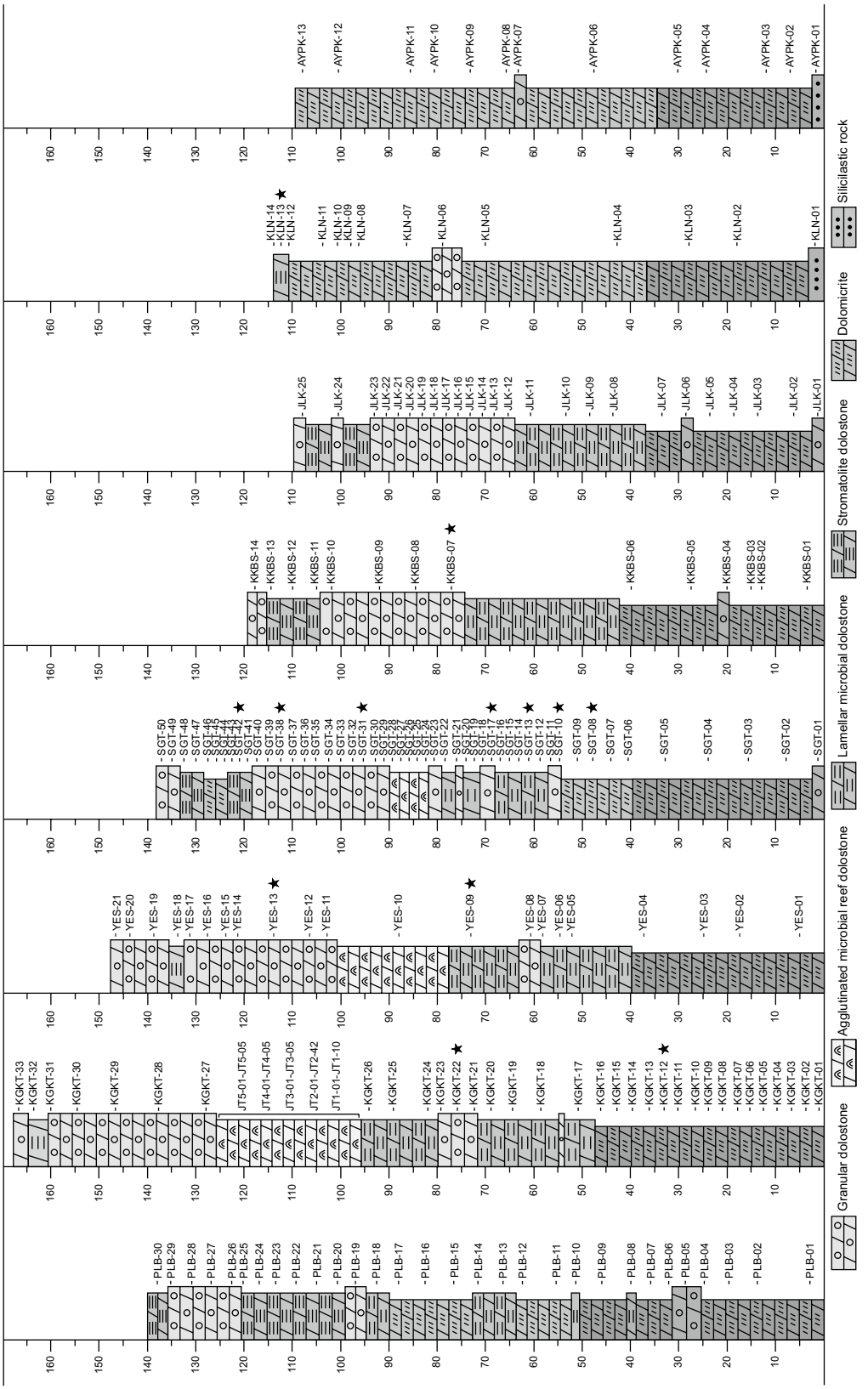

Fig. 4 Lithologic columns of the Xiaoerbulak Formation from the eight sections indicating the sampling points and serial numbers for all samples. Samples collected for in situ geochemical experiments are indicated with black stars

4.1 Replacive dolomites (Rd)

4.1.1 Micritic–microspar dolomites (Rd1)

Rd1 commonly show micritic–microspar crystals smaller than 30 μm. These dolomites generally occur in the sedimentary fabrics of Xiaoerbulak dolostones, which have undergone complete dolomitization and weak recrystallization from precursor carbonates, including (1) micritic dolostones (Fig. 6a), (2) dark layers of laminated microbial and stromatolite dolostones (Fig. 6b, c), (3) agglutinated microbial reef dolostones (Fig. 6d), and (4) grains of dolograinstone (Fig. 6e, f).

4.1.2 Pseudospar, non-planar dolomites (Rd2)

Rd2 usually exhibit pseudospar crystals ranging from 30 to 100 μm with non-planar textures. These dolomites commonly exist in the sedimentary fabrics different from that of Rd1, including (1) bright layers of laminated microbial and stromatolite dolostones (Fig. 6b, c), and (2) cements of dolograinstone (Fig. 6e, f). These sedimentary fabrics have also undergone complete dolomitization and weak recrystallization from precursor carbonates. Furthermore, Rd2 can occur in slightly recrystallized zones of those sedimentary fabrics (Fig. 6g, h).

4.1.3 Fine-to-medium crystalline, planar-s dolomites (Rd3)

Rd3 generally display fine-to-medium crystals ranging from 100 to 300 μm with planar subhedral textures. These dolomites usually appear in the zones that have undergone much stronger recrystallization (Fig. 6h). Furthermore, the sedimentary fabrics can be completely replaced by Rd3 through strong recrystallization (Fig. 6i).

4.2 Pore-filling dolomites (Fd)

4.2.1 Fine-to-medium crystalline, planar-e dolomites (Fd1)

Fd1 are generally planar euhedral crystals ranging from 100 to 500 μm with diamond textures (Fig. 7a–f, h–i). These dolomites show either clear and homogeneous or with cloudy cores and clear rims (Fig. 7a–f, h–i), with all dolomites displaying sharp to slightly sweeping extinctions. Fd1 occur as the first generation of filling minerals lining the smooth walls of fractures and dissolution pores, and they generally hackly arrange along the walls and only account for small proportions of the spaces (Fig. 7c–e, h–i). These dolomites can be followed by Fd2 abruptly, resulting in complete occlusion of pores (Fig. 7h–i).

4.2.2 Coarse crystalline, non-planar-a saddle dolomites (Fd2)

Fd2 usually show non-planar anhedral crystals ranging from 0.5 to 3 mm with saddle crystal textures (Fig. 7g–i). These dolomites display either cloudy or with thick cloudy cores and fairly thin clear rims, with all dolomites showing curved crystals with cambered cleavages (Fig. 7g–i) and undulating extinctions. Fd2 occur as the second generation of filling minerals growing over Fd1 (Fig. 7h–i) and are the innermost minerals occluding the remaining pore spaces that have been partially or not occluded by Fd1.

4.3 Late-stage filling calcites (Fc)

Filling calcites (Fc) are stained to jacinth by alizarin red-S (Fig. 7c) and are characterized by planar euhedral crystal textures with planar cleavages. These calcites are the latest fracture infills postdating all dolomites, which may have successively precipitated after the Fds; the transition between Fds and Fc is generally abrupt (Fig. 7c). However, Fc are only found in the vugs and fractures of dolostones subjected to weathering and leaching.

4.4 Reservoir spaces

4.4.1 Types and distributions

Reservoir spaces are mainly secondary pores due to dolomitization, recrystallization, and dissolution, which have altered the primary pores and generated new dissolution pores (Fig. 8). The reservoir spaces can be divided into 3 types according to genesis: (1) fabric selective dissolution pores, which are generated by altering a distinct sedimentary fabric, and the boundaries of these reservoir spaces do not cut through another fabric, including intraparticle dissolution pores (Fig. 8a, b), interparticle dissolution pores (Fig. 8b, c), intercrystalline dissolution pores (Fig. 8c, d), and bed-parallel dissolution pores (Fig. 8g); (2) fabric non-selective dissolution pores, which are generated by dissolving diverse fabrics, and the boundaries of these reservoir spaces generally cut through at least two kinds of fabrics, mainly enhanced dissolution pores (Fig. 8f–i); (3) fractures, which are generated by structural deformation (Fig. 8c).

4.4.2 Filling situation

Petrography observations indicate that no Fc developed in any reservoir spaces of fresh dolostones. Furthermore, fabric selective dissolution pores are seldom occupied with Fds (Fig. 8a–g). In contrast, Fabric non-selective dissolution pores are frequently occupied by one or two types of Fds (Figs. 7d–f, h, i, 8f–i).

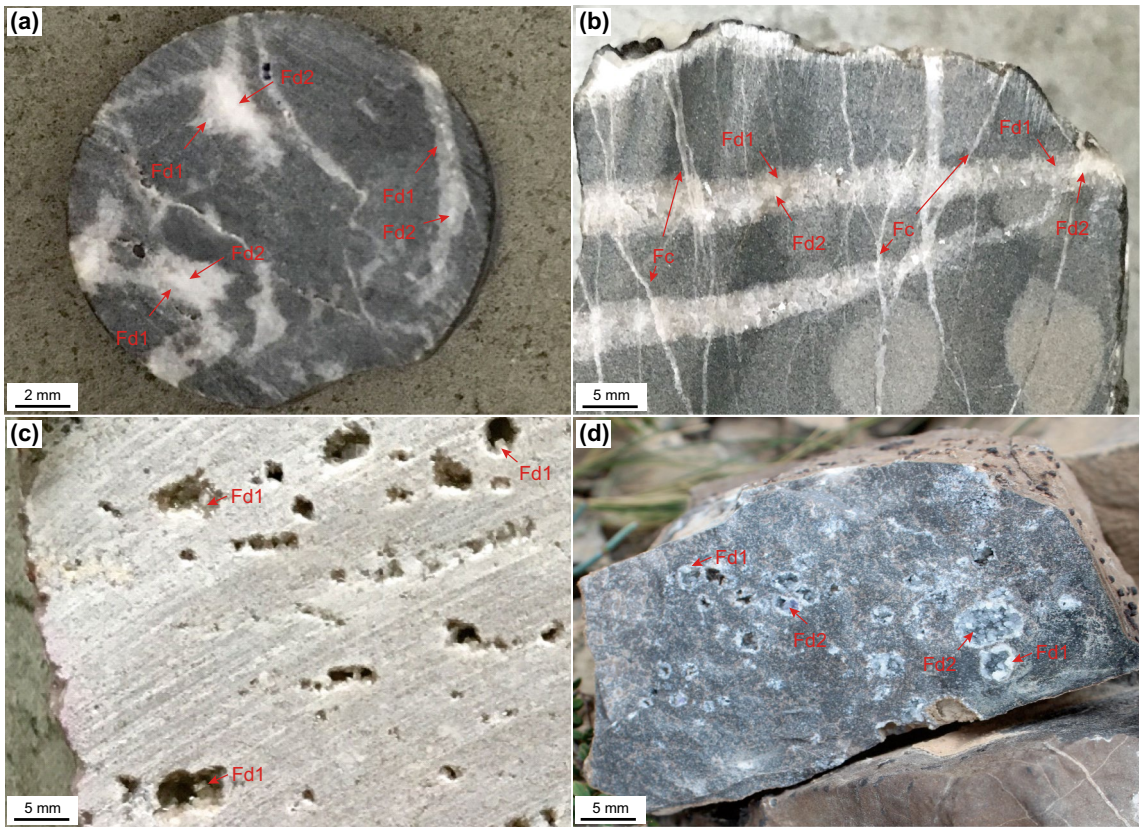

Fig. 5 Photographs of samples showing the distributions and intergrowth relationships of different pore-filling dolomites and filling calcites in the dolostones of the Lower Cambrian Xiaoerbulak Formation. **a** Fd1 and Fd2 in the fractures of micritic dolostones. **b** Fd1 and Fd2 and Fc in the fractures of micritic dolostones. **c** Fd1 in the dissolution pores of dolograinstones. **d** Fd1 in the dissolution pores of micritic dolostones

The Fd2 are only found in occlusive enhanced dissolution pores, showing a paragenetic relationship with Fd1 (Fig. 7h, i). Only Fd1 develop in the existing enhanced dissolution pores; they primarily grow around the inner walls and only take up small proportions of these reservoir spaces (Figs. 7d–f, 8f–i). Hence, large proportions of the reservoir spaces can be preserved if Fd2 do not develop. However, the appearance of Fd2 results in the loss of these reservoir spaces because they completely occlude the remaining reservoir spaces that have not been filled by Fd1 (Fig. 7g–i).

5 In situ geochemistry

5.1 In situ testing results

Only a single spot was tested in each dolomite grain with homogeneous crystal features. In addition, cloudy cores and clear rims were separately tested for each Fd grain with heterogeneous crystal features. In total, 66 spots in 13 samples were tested, including 12 spots for Rd1 (marked in gray), 12 spots for Rd2 (marked in yellow), 8 spots for Rd3 (marked in orange, including Fd1 cores with geochemical propertied similar to that of Rd3), 25 spots for Fd1 (marked in green), and 9 spots for Fd2 (marked in blue) (Fig. 9). All test results are provided in Table 1. Note that the cloudy cores of heterogeneous Fd1 in SGT-10-6 and SGT-17-1, 4 are marked in orange (Fig. 9d, h) because they show geochemical characteristics similar to Rd3 rather than Fd1. However, the cloudy cores and clear rims of heterogeneous Fd2 in KLN-13 (Fig. 9m) and SGT-08 (Fig. 9p) show the same geochemical characteristics to those of homogeneous Fd2. Detailed test results are described as follows in Table 1.

5.2 Trace elemental composition

5.2.1 Mn contents

Mn contents of all samples range from 50.7 to 529.8 ppm (mean = 130.8 ppm, $n = 66$). The Mn contents of Rd1, Rd2, and Rd3 are nearly the same, vary between 59.8 and 103.7 ppm (mean = 74.8 ppm, $n = 12$), 58.9–110.9 ppm (mean = 76.2 ppm, $n = 12$) and 50.7–122.7 ppm (mean = 81.7 ppm, $n = 8$), respectively. Mn contents of Fds are much higher than those of Rds. The Mn contents of Fd1 and Fd2 range from 96.9 to 409.7 ppm (mean = 172.5 ppm,

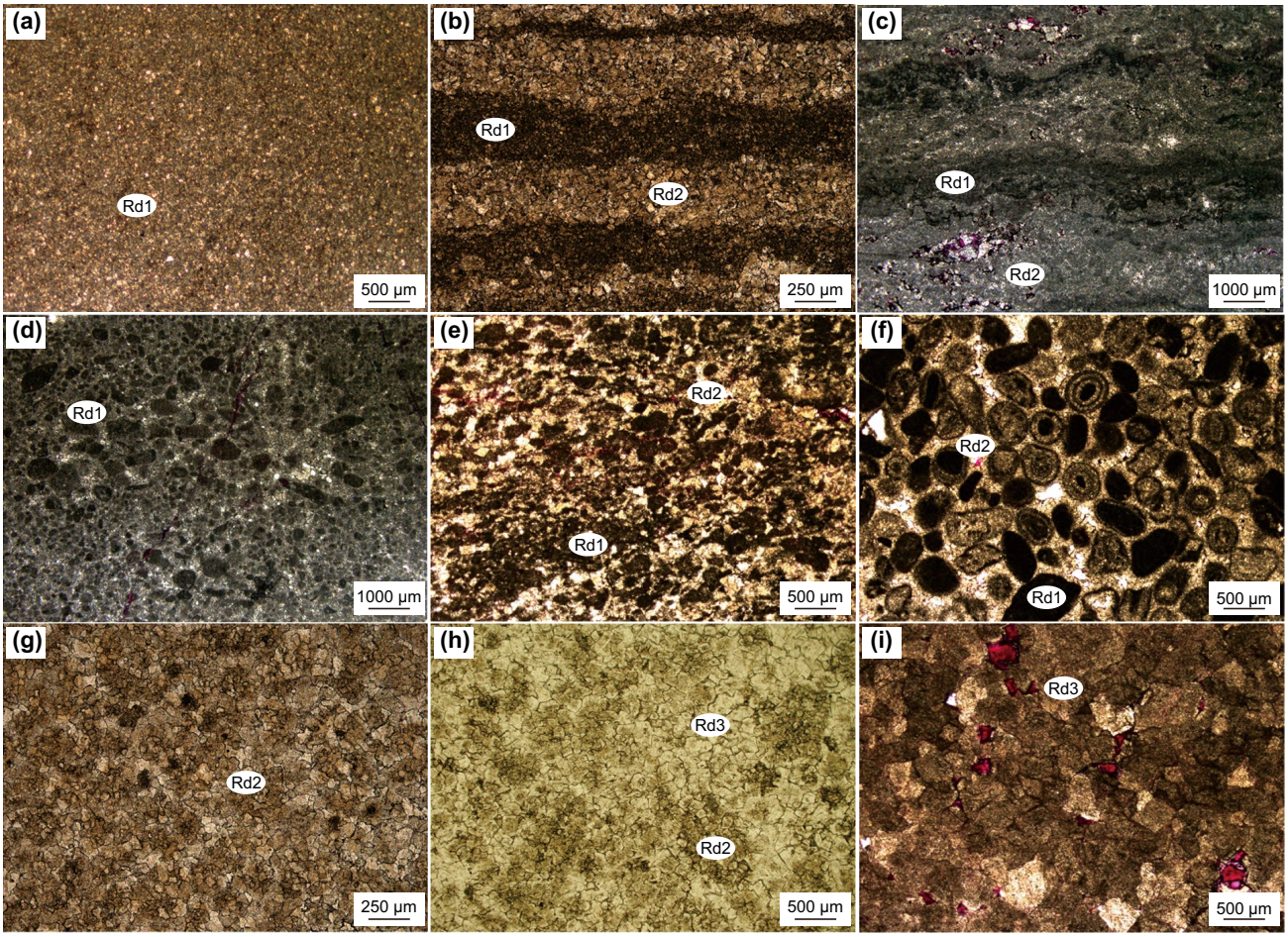

Fig. 6 Photomicrographs showing the textures and distributions of different replacive dolomites. **a** Rd1 in the micritic dolostones (KKBS-05). **b** Rd1 and Rd2 in the laminated microbial dolostones (PLB-13). **c** Rd1 and Rd2 in the stromatolite dolostones (SGT-47). **d** Rd1 in the agglutinated microbial dolostones (JT2-17). **e**, **f** Rd1 and Rd2 in the dolograinstone (KLN-06 and JLK-24). **g** Rd2 in the slightly recrystallized zones of micritic dolostones (KLN-02). **h** Rd2 and Rd3 in the heterogeneous recrystallized zones of dolograinstone (KGKT-27). **i** Rd3 in the strongly recrystallized zones of dolograinstone (KKBS-09)

$n = 25$) and 126.2–529.8 ppm (mean = 205.9 ppm, $n = 9$) (Table 1) (Fig. 10).

5.2.2 Fe contents

Fe contents of all samples vary from 129.3 to 1741.8 ppm (mean = 508.1 ppm, $n = 66$). The Fe contents range from 288.4 to 1741.8 ppm for Rd1 (mean = 792.5 ppm, $n = 12$), 184.8–801.3 ppm for Rd2 (mean = 502.0 ppm, $n = 12$), 190.7–529.7 ppm for Rd3 (mean = 329.6, $n = 8$), 166.3–1568.3 ppm (mean = 550.1 ppm, $n = 25$) for Fd1, and 129.3–220.9 ppm (mean = 178.6 ppm, $n = 9$) for Fd2 (Table 1). Among Rds, Rd1 show the highest average Fe content and Rd3 dolomites display the lowest Fe content. For Fds, Fd1 show much higher average Fe content than Fd2 (Fig. 10a).

5.2.3 Sr contents

Sr contents of all samples vary from 14.3 to 69.5 ppm (mean = 27.7 ppm, $n = 66$), including 23.6–52.6 ppm for Rd1 (mean = 33.1 ppm, $n = 12$), 21.3–37.3 ppm for Rd2 (mean = 27.0 ppm, $n = 12$), 21.5–28.5 ppm for Rd3 (mean = 24.2 ppm, $n = 8$), 14.3–31.8 ppm (mean = 22.2 ppm, $n = 25$) for Fd1, and 29.1–69.5 ppm (mean = 42.1 ppm, $n = 9$) for Fd2 (Table 1). Rd1 show an average Sr content slightly higher than Rd2, and Rd2 slightly higher than Rd3. And the average Sr content of Fd2 is nearly twice of Fd1 (Fig. 10b).

5.2.4 Ba contents

Ba contents of all samples vary from 0.06 to 4.56 ppm (mean = 0.79 ppm, $n = 66$), respectively, ranging from 0.74 to 4.56 ppm (mean = 2.16 ppm, $n = 12$) for Rd1, 0.34–2.65 ppm

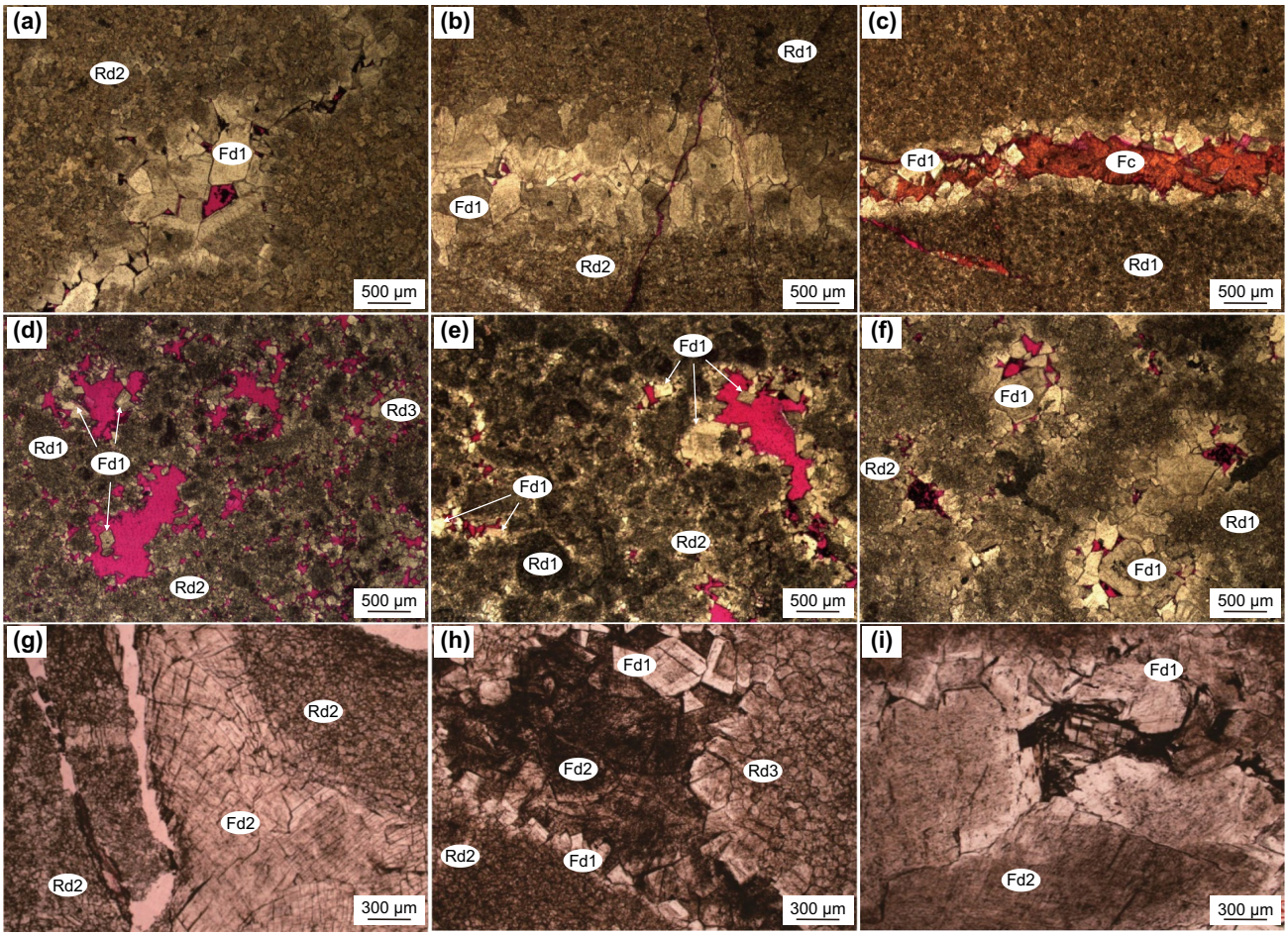

Fig. 7 Photomicrographs showing the textures and distributions of different dolomites and filling calcites. **a**, **b** Fd1 in the fractures of micritic dolostones (SGT-06 and KGKT-09). **c** Fd1 and Fc in the fractures of micritic dolostones (KGKT-05). **d** Fd1 on the inner walls of dissolution pores in dolograinstone (YES-16). **e** Fd1 on the inner walls of dissolution pores in dolograinstone (YES-12). **f** Fd1 filling in the dissolution pores of dolograinstone (SGT-30). **g** Fd2 in the fractures of micritic dolostones (KLN-03). **h**, **i** The intergrowth relationship of Fd1 and Fd2 in the dissolution pores of micritic dolostones (KGKT-12 and SGT-08)

(mean = 0.93 ppm, $n = 12$) for Rd2, 0.24–1.59 ppm (mean = 0.61 ppm, $n = 8$) for Rd3, 0.07–0.57 ppm (mean = 0.21 ppm, $n = 25$) for Fd1, and 0.06–1.05 ppm (mean = 0.53 ppm, $n = 9$) for Fd2 (Table 1). Among the Rds, Rd1 show the highest average Ba content and Rd3 display the lowest. Of the Fds, Fd2 show a higher average Ba content than Fd1 (Fig. 10c).

5.3 REE (rare-earth elements) composition

5.3.1 Total REE abundances

Total REE abundances (ΣREE) of all samples range from 0.96 to 31.87 ppm (mean = 6.15 ppm, $n = 66$), including 1.19–3.25 ppm (mean = 2.07 ppm, $n = 12$) for Rd1, 1.12–4.14 ppm for Rd2 (mean = 1.86 ppm, $n = 12$), 0.96–4.71 ppm for Rd3 (mean = 1.85 ppm, $n = 8$), 1.96–31.87 ppm for Fd1 (mean = 8.83 ppm, $n = 25$), and 7.08–24.36 ppm for Fd2 (mean = 13.68 ppm, $n = 9$) (Table 1). Rd1, Rd2, and Rd3 have similar average ΣREE,

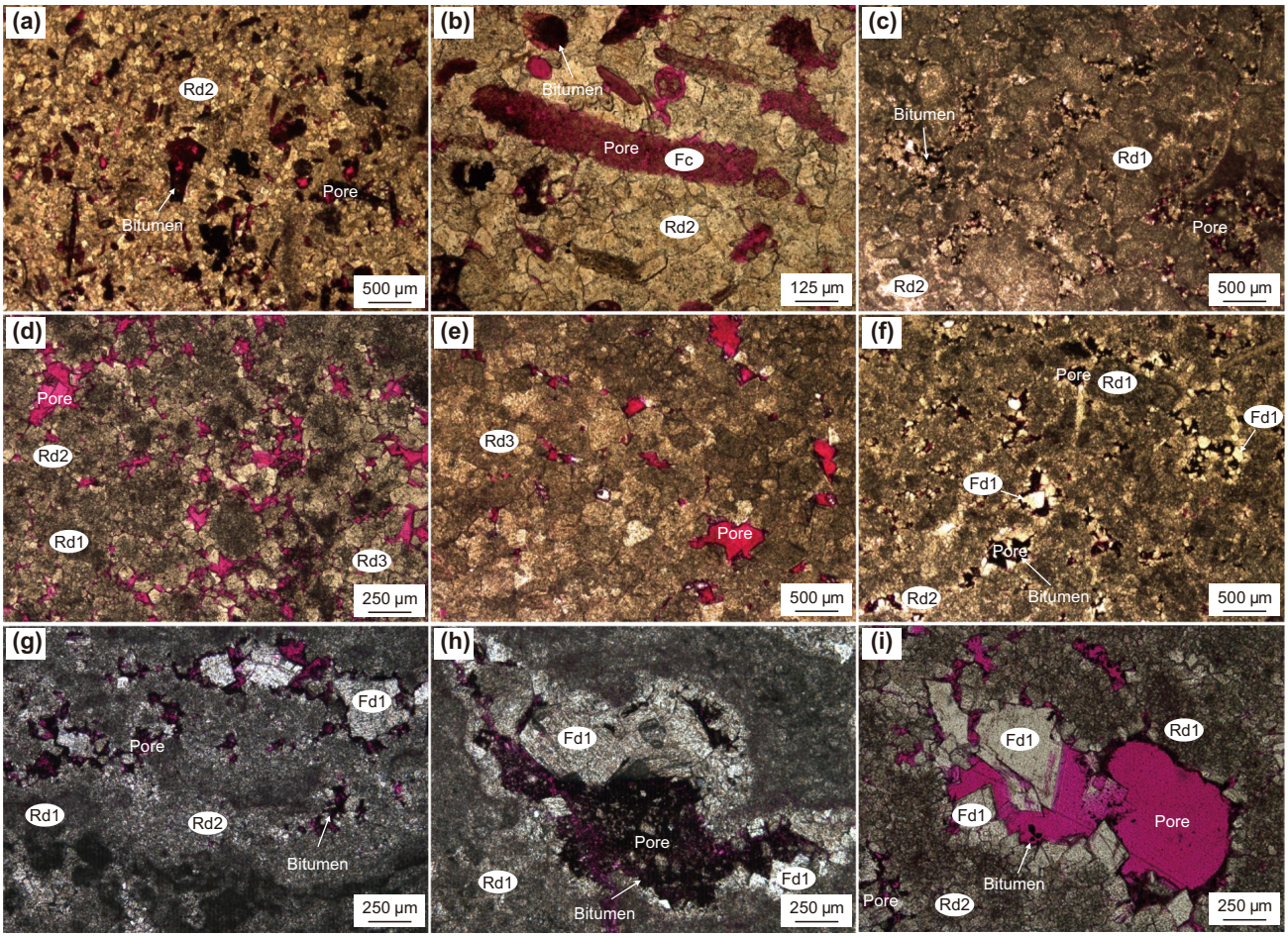

Fig. 8 Photomicrographs showing types, distributions, and filling conditions of reservoir spaces in the dolostones of the Lower Cambrian Xiaoerbulak Formation. **a**, **b** Intraparticle dissolution pores without pore-filling dolomites in dolograinstone (JLK-01). **c** Interparticle dissolution pores in dolograinstone (YES-19). **d** Interparticle and intercrystalline dissolution pores in dolograinstone (JLK-23). **e** Intercrystalline dissolution pores in strongly recrystallized dolostones (KKBS-08). **f** Enhanced dissolution pores in dolograinstone (KGKT-30). **g** Bed-parallel dissolution pores in stromatolite dolostones (SGT-41). **h** Dissolution pores in stromatolite dolostones (SGT-43). **i** Dissolution pores in slightly recrystallized dolograinstone (JLK-13)

and Fd2 show higher average ΣREE than Fd1. Generally, Rds show much lower ΣREE than Fds (Fig. 11).

5.3.2 Ce and Eu anomaly values

Ce anomaly values were calculated using the relationship $Ce/Ce^* = Ce_{SN}/(0.5La_{SN} + 0.5Pr_{SN})$ (Bau et al. 1996). The Ce anomaly values of different types of dolomites, respectively, range from 0.83 to 1.11 (mean = 1.00, $n = 12$) for Rd1, 0.77–1.17 (mean = 1.03, $n = 12$) for Rd2, 0.69–1.21 (mean = 0.92, $n = 8$) for Rd3, 0.94–1.76 (mean = 1.30, $n = 25$) for Fd1, and 0.85 to 0.97 (mean = 0.92, $n = 9$) for Fd2. The Rds and Fd2 show indistinct, even no anomaly features, and Fd1 exhibit weak positive Ce anomaly features (Table 1).

Eu anomaly values were calculated using the relationship $Eu/Eu^* = Eu_{SN}/(0.67Sm_{SN} + 0.33Tb_{SN})$ (Bau et al. 1996). The Rds show rather weak Eu anomaly features, with the Eu anomaly values of Rd1, Rd2, and Rd3 varying from 0.79 to 1.48 (mean = 1.05, $n = 11$), 0.87–1.25 (mean = 1.04, $n = 9$), and 0.89–1.59 (mean = 1.14, $n = 5$), respectively. Fd1 show weak Eu anomaly features with a value range from 0.76 to 1.28 (mean = 1.06, $n = 25$), and Fd2 show clear positive Eu anomaly features with a value range from 1.32 to 2.90 (mean = 1.89, $n = 9$) (Table 1).

5.3.3 REE distribution patterns

The REE distribution patterns are illustrated by normalizing the REEs against PAAS (Mclennan, 1989). Rd1, Rd2, and Rd3 all show slightly left-leaning REE patterns with minor light-REE (LREE) depletion and heavy-REE (HREE) enrichment (Fig. 12a–c). Fd1 display roof-shaped (upward convex) REE patterns with notable middle-REE (MREE)

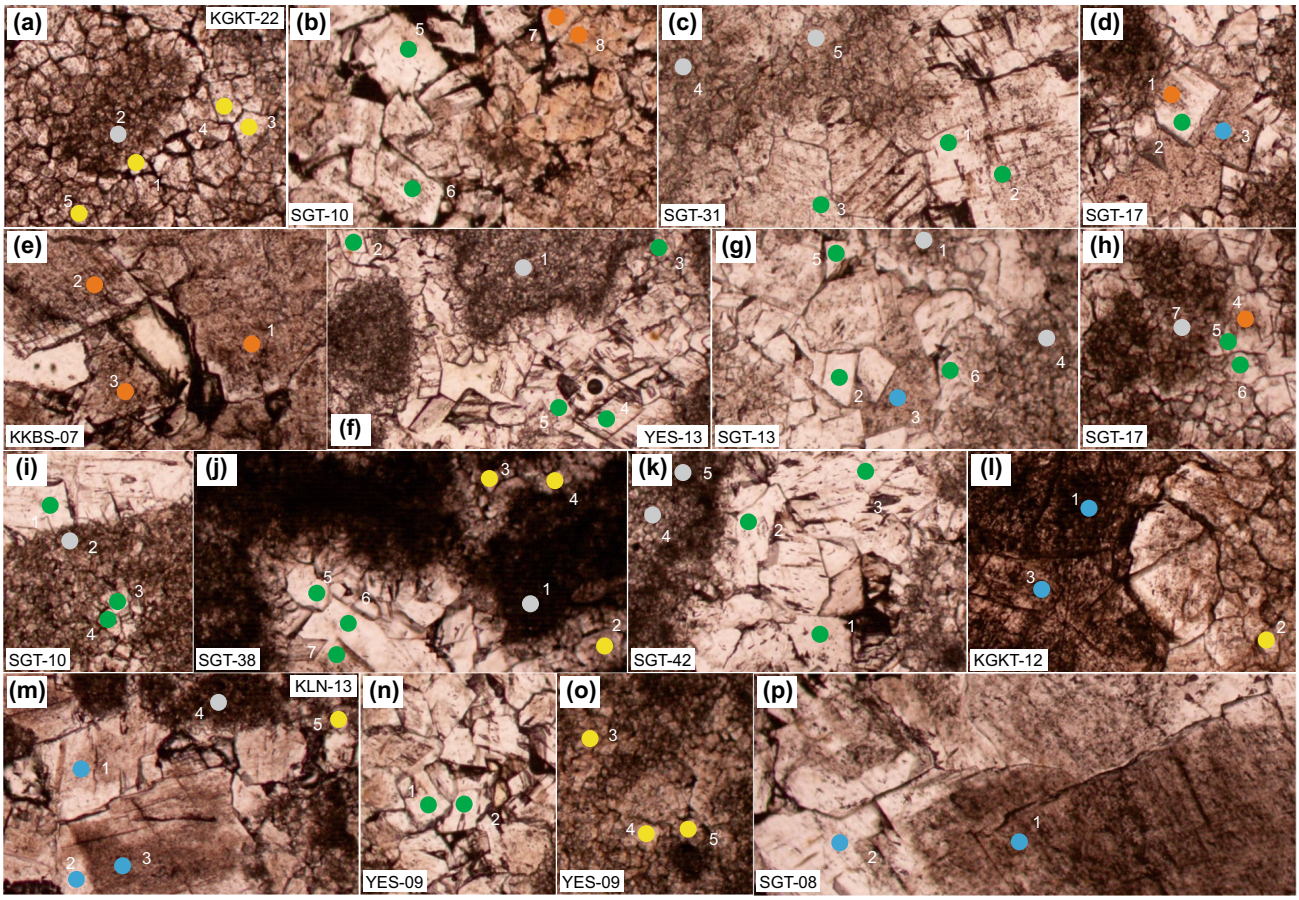

Fig. 9 Photomicrographs showing the 66 test locations in the 13 representative microprobe thin sections for in situ geochemical experiment. Gray: Rd1, yellow: Rd2, orange: Rd3 and core of Fd1 with geochemical features similar to Rd3 (the core of Fd1 dolomites in SGT-10-6, SGT-17-1, 4), green: Fd1 and the rim of Fd1 (the rim of Fd1 dolomites in SGT-17-2, 5, and blue: Fd2

enrichment and depletion of LREE and HREE (Fig. 12d–f). Approximately, half of the Fd2 show slightly right-leaning REE patterns with clear positive Eu anomalies (Eu/Eu* ranging from 1.82 to 2.90, mean = 2.36, $n = 5$) (Fig. 12g) and the other half exhibit significantly right-leaning REE patterns with moderate positive Eu anomalies (Eu/Eu* ranging from 1.32 to 1.61, mean = 1.52, $n = 4$) (Fig. 12h).

6 Interpretation and discussion

6.1 Diagenetic fluids of different dolomites

Based on petrography and geochemical properties of the samples, we interpret the types, nature, and origin of the fluids which formed different types of dolomites.

6.1.1 Origin of replacive dolomites (Rd)

All replacive dolomites may have similar or even the same origin. Rds are distributed in the sedimentary fabrics and recrystallized zones of the Xiaoerbulak dolostones, indicate that these dolomites are likely originated from precursor carbonates, and experienced dolomitization and recrystallization under the influence of dolomitizing fluids. All Rds show nearly the same REE distribution patterns (Fig. 12a–c), and only slight changes in trace elemental composition can be distinguished among them (Fig. 10a–c). Therefore, we propose that the Rd1, Rd2, and Rd3 have similar or even the same origin.

The dolomitizing fluids of Rds may be related to ancient seawater. Rd1, Rd2, and Rd3 show slightly left-leaning REE patterns and slightly positive or no Ce anomalies (Fig. 12a–c) and show inheritance from seawater or precursor carbonates (Alibo and Nozaki 1999; Mclennan 1989; Zhang et al. 2008; Zhao and Jones 2013). Based on the lack of Ce anomalies (Table 1), low ΣREE (Fig. 11), moderate-to-high Fe, and low Mn (Fig. 10a), dolomitizing fluids should be weakly oxidizing (Morford and Emerson 1999) and have non-hydrothermal properties (Chen et al. 2009a; Middleton et al. 1993). Low Mn abundances also imply that meteoric waters and deep fluids did not

Table 1 LA-ICP-MS in situ trace and rare-earth element data of Rd and Fd

Sample (test spot)	Type	Mn	Fe	Zn	Sr	Y	Ba	La	Ce	Pr	Nd	Sm	Eu	Gd	Tb
KGKT-22(2)	Rd1	72	1742	11	24	0.29	3.2	0.27	0.57	0.066	0.19	0.043		0.037	0.012
YES-13(1)	Rd1	77	387	15	33	0.47	0.84	0.52	1.1	0.12	0.49	0.094	0.019	0.096	0.015
SGT-10(2)	Rd1	78	514	10	24	0.61	0.92	0.52	1.3	0.18	0.71	0.12	0.028	0.11	0.020
SGT-13(1)	Rd1	63	478	8.9	29	0.34	2.4	0.38	0.72	0.088	0.31	0.074	0.014	0.038	0.009
SGT-13(4)	Rd1	77	288	8.0	33	0.46	0.74	0.38	0.80	0.097	0.38	0.048	0.014	0.048	0.007
SGT-17(7)	Rd1	60	863	13	26	0.37	2.0	0.43	0.89	0.093	0.40	0.069	0.010	0.047	0.008
SGT-31(4)	Rd1	72	1312	12	28	0.53	1.8	0.30	0.64	0.083	0.28	0.061	0.013	0.054	0.010
SGT-31(5)	Rd1	66	505	8.5	28	0.28	1.1	0.24	0.51	0.051	0.21	0.042	0.011	0.035	0.007
SGT-38(1)	Rd1	99	590	9.9	30	0.53	1.4	0.42	0.94	0.097	0.45	0.083	0.017	0.065	0.014
SGT-42(4)	Rd1	63	1029	14	30	0.46	3.5	0.47	0.93	0.093	0.43	0.076	0.015	0.065	0.013
SGT-42(5)	Rd1	104	925	15	37	0.54	3.6	0.48	1.0	0.11	0.49	0.086	0.017	0.080	0.016
KLN-13(4)	Rd1	67	877	9.8	53	0.32	4.6	0.45	0.75	0.087	0.33	0.082	0.017	0.11	0.013
KGKT-12(2)	Rd2	109	185	8.0	28	0.82	2.7	1.0	1.6	0.19	0.75	0.14	0.032	0.11	0.027
KGKT-22(1)	Rd2	89	594	7.0	26	0.28	0.79	0.27	0.64	0.068	0.30	0.063	0.012	0.050	0.012
KGKT-22(3)	Rd2	59	523	6.1	22	0.20	0.56	0.22	0.47	0.051	0.19	0.047	0.011	0.038	
KGKT-22(4)	Rd2	63	555	6.3	22	0.23	0.58	0.21	0.46	0.052	0.21	0.055	0.015	0.038	0.012
KGKT-22(5)	Rd2	65	784	7.3	23	0.22	0.71	0.25	0.50	0.051	0.23	0.056	0.011	0.050	0.011
YES-09(3)	Rd2	75	373	6.6	36	0.38	0.95	0.28	0.69	0.079	0.31	0.061	0.013	0.043	0.008
YES-09(4)	Rd2	111	252	6.5	29	0.52	1.1	0.50	1.3	0.16	0.63	0.10	0.024	0.076	0.019
YES-09(5)	Rd2	69	269	6.8	37	0.32	0.69	0.27	0.61	0.073	0.29	0.069	0.015	0.057	
SGT-38(2)	Rd2	63	488	6.3	27	0.23	0.34	0.20	0.44	0.052	0.25	0.039	0.009	0.037	0.009
SGT-38(3)	Rd2	60	581	7.7	24	0.23	0.93	0.24	0.48	0.039	0.21	0.037	0.007	0.035	
SGT-38(4)	Rd2	61	619	7.9	21	0.27	0.54	0.24	0.53	0.052	0.26	0.049	0.009	0.045	0.007
KLN-13(5)	Rd2	90	801	7.4	30	0.50	1.3	0.78	1.5	0.15	0.55	0.062	0.021	0.076	0.019
SGT-10(7)	Rd3	55	191	6.7	25	0.31	1.6	0.38	0.80	0.091	0.32	0.048	0.013	0.054	
SGT-10(8)	Rd3	65	298	7.4	24	0.29	0.79	0.38	0.73	0.076	0.34	0.043	0.011	0.059	0.008
SGT-10(6)	Fd1 core	73	244	5.4	22	0.72	0.41	0.79	2.1	0.25	0.86	0.19	0.035	0.12	0.021
SGT-17(1)	Fd1 core	57	530	8.1	27	0.28	0.44	0.36	0.71	0.075	0.36	0.063	0.011	0.051	0.009
SGT-17(4)	Fd1 core	51	382	6.5	29	0.21	0.53	0.31	0.60	0.066	0.25	0.057	0.010	0.043	
KKBS-07(1)	Rd3	121	380	7.0	23	0.39	0.24	0.28	0.39	0.054	0.19	0.030	0.008	0.028	0.008
KKBS-07(2)	Rd3	123	331	7.3	22	0.39	0.53	0.24	0.39	0.069	0.16	0.067		0.054	0.006
KKBS-07(3)	Rd3	110	281	7.9	23	0.32	0.32	0.21	0.35	0.044	0.15	0.032	0.011	0.049	0.006
YES-09(1)	Fd1	129	200	6.5	18	0.55	0.090	0.35	1.3	0.19	0.89	0.18	0.026	0.15	0.024
YES-09(2)	Fd1	119	231	5.3	24	0.65	0.070	0.060	0.71	0.18	0.92	0.25	0.035	0.13	0.025
YES-13(2)	Fd1	140	553	7.3	33	1.0	0.37	0.63	2.0	0.26	1.1	0.23	0.053	0.20	0.024
YES-13(3)	Fd1	165	299	8.1	21	1.1	0.50	0.16	0.91	0.16	0.87	0.20	0.040	0.23	0.032
YES-13(4)	Fd1	150	214	6.8	19	0.53	0.080	0.11	0.53	0.11	0.67	0.17	0.035	0.11	0.018
YES-13(5)	Fd1	160	559	8.2	28	1.2	0.070	0.53	2.0	0.27	1.3	0.22	0.051	0.32	0.035
SGT-10(1)	Fd1	323	1091	5.1	22	6.1	0.13	2.7	9.3	1.8	8.4	1.9	0.33	1.5	0.23
SGT-10(3)	Fd1	128	476	6.8	22	1.3	0.47	0.71	1.8	0.33	1.5	0.32	0.065	0.27	0.043
SGT-10(4)	Fd1	167	612	7.0	21	1.9	0.38	0.91	2.6	0.52	2.5	0.55	0.12	0.41	0.054
SGT-10(5)	Fd1	310	1014	5.8	19	4.9	0.090	3.9	11	1.9	9.2	1.9	0.36	1.5	0.19
SGT-13(2)	Fd1	116	326	7.5	31	0.64	0.43	0.60	2.0	0.27	1.1	0.25	0.057	0.21	0.029
SGT-13(5)	Fd1	109	184	6.6	25	1.2	0.14	1.1	4.1	0.59	2.4	0.49	0.095	0.39	0.056
SGT-13(6)	Fd1	99	318	6.8	27	0.53	0.41	0.56	1.6	0.20	0.94	0.22	0.046	0.18	0.027
SGT-17(2)	Fd1 rim	105	166	7.2	22	0.87	0.57	1.0	2.6	0.31	1.3	0.28	0.048	0.19	0.032
SGT-17(5)	Fd1 rim	99	302	7.1	25	0.91	0.10	0.63	2.1	0.30	1.2	0.30	0.049	0.21	0.033
SGT-17(6)	Fd1	97	586	6.6	32	0.75	0.17	0.79	2.6	0.35	1.4	0.28	0.051	0.22	0.036
SGT-31(1)	Fd1	113	370	6.4	15	0.95	0.090	0.29	1.1	0.21	0.89	0.18	0.046	0.17	0.036

Table 1 (continued)

Sample (test spot)	Type	Mn	Fe	Zn	Sr	Y	Ba	La	Ce	Pr	Nd	Sm	Eu	Gd	Tb
SGT-31(2)	Fd1	298	745	6.6	20	3.1	0.13	1.8	5.0	0.98	4.5	0.92	0.15	0.53	0.10
SGT-31(3)	Fd1	410	1337	8.0	21	5.1	0.44	2.7	6.1	1.1	5.2	1.0	0.21	0.80	0.14
SGT-38(5)	Fd1	132	375	5.9	15	1.3	0.060	1.3	3.8	0.56	2.4	0.46	0.084	0.27	0.039
SGT-38(6)	Fd1	138	369	6.2	14	1.1	0.060	0.31	1.6	0.27	1.5	0.33	0.065	0.27	0.031
SGT-38(7)	Fd1	386	1568	6.6	21	3.3	0.15	1.3	4.2	0.77	3.7	0.85	0.15	0.79	0.089
SGT-42(1)	Fd1	127	666	6.5	21	0.77	0.070	0.91	2.9	0.38	1.6	0.27	0.063	0.23	0.036
SGT-42(2)	Fd1	166	536	6.2	19	1.4	0.090	1.4	4.2	0.69	2.8	0.48	0.10	0.42	0.057
SGT-42(3)	Fd1	129	659	6.0	21	1.2	0.080	0.87	3.2	0.43	2.0	0.35	0.071	0.25	0.040
KGKT-12(1)	Fd2	162	143	8.0	37	4.4	0.33	4.1	7.3	0.87	3.8	0.70	0.21	0.56	0.082
KGKT-12(3)	Fd2	138	129	6.1	44	2.3	0.34	2.0	3.4	0.42	1.8	0.36	0.088	0.26	0.043
SGT-08(1)	Fd2 core	222	205	6.7	48	2.3	0.65	1.6	3.1	0.40	1.6	0.34	0.19	0.34	0.047
SGT-08(2)	Fd2 rim	126	211	8.0	47	1.8	0.060	1.4	2.8	0.34	1.5	0.27	0.14	0.22	0.036
SGT-13(3)	Fd2	151	146	6.8	69	1.2	1.1	2.2	4.4	0.53	2.1	0.42	0.16	0.37	0.048
SGT-17(3)	Fd2	145	185	7.4	32	1.1	0.85	1.5	3.0	0.38	1.6	0.26	0.085	0.23	0.028
KLN-13(1)	Fd2	193	171	7.5	29	2.4	0.41	5.4	11	1.1	4.2	0.67	0.20	0.62	0.087
KLN-13(2)	Fd2 rim	187	221	5.6	36	2.1	0.24	5.9	11	1.1	4.2	0.73	0.19	0.59	0.071
KLN-13(3)	Fd2 core	530	197	7.4	38	1.4	0.84	3.2	6.0	0.64	2.5	0.40	0.12	0.35	0.049

Sample (test spot)	Type	Dy	Ho	Er	Tm	Yb	Lu	Th	U	∑REE	Ce/Ce^*	Eu/Eu^*
KGKT-22(2)	Rd1	0.055	0.012	0.029	0.005	0.028	0.004	0.088	0.99	1.3	0.99	
YES-13(1)	Rd1	0.071	0.016	0.047		0.034	0.005	0.12	0.38	2.7	1.0	0.99
SGT-10(2)	Rd1	0.10	0.024	0.068	0.010	0.050		0.11	0.40	3.3	1.1	1.1
SGT-13(1)	Rd1	0.038	0.011	0.028		0.039	0.007	0.10	1.4	1.8	0.91	1.0
SGT-13(4)	Rd1	0.047	0.014	0.040	0.006	0.049	0.006	0.053	0.57	1.9	0.99	1.5
SGT-17(7)	Rd1	0.059	0.009	0.024	0.006	0.049	0.007	0.083	1.1	2.1	1.0	0.79
SGT-31(4)	Rd1	0.055	0.014	0.034	0.006	0.034	0.007	0.18	0.75	1.6	0.99	1.0
SGT-31(5)	Rd1	0.040	0.011		0.005	0.024	0.005	0.054	0.53	1.2	1.0	1.3
SGT-38(1)	Rd1	0.076	0.014	0.039	0.006	0.035	0.006	0.20	0.34	2.3	1.1	0.98
SGT-42(4)	Rd1	0.065	0.014	0.039	0.005		0.006	0.092	0.49	2.2	0.98	0.94
SGT-42(5)	Rd1	0.085	0.019	0.045	0.007	0.054	0.007	0.24	0.42	2.5	1.0	0.91
KLN-13(4)	Rd1	0.10	0.015	0.045	0.005	0.035		0.11	0.30	2.0	0.83	1.0
KGKT-12(2)	Rd2	0.11	0.021	0.063	0.009	0.058	0.008	0.043	0.62	4.1	0.77	1.1
KGKT-22(1)	Rd2	0.061	0.011	0.028	0.005			0.058	0.58	1.5	1.1	0.87
KGKT-22(3)	Rd2	0.049	0.011		0.005	0.027	0.004	0.054	0.71	1.1	1.0	
KGKT-22(4)	Rd2	0.049	0.008	0.028		0.025		0.074	0.80	1.2	1.0	1.2
KGKT-22(5)	Rd2	0.046	0.012	0.023	0.004		0.004	0.056	0.75	1.3	0.98	0.89
YES-09(3)	Rd2	0.051	0.010	0.041	0.007	0.038	0.006	0.077	2.7	1.6	1.1	1.1
YES-09(4)	Rd2	0.075	0.014	0.056	0.006	0.062	0.006	0.052	2.3	3.1	1.2	1.1
YES-09(5)	Rd2	0.055	0.009	0.040	0.006	0.034	0.006	0.057	2.7	1.5	1.1	
SGT-38(2)	Rd2	0.046	0.009	0.022	0.004	0.026	0.005	0.031	0.32	1.2	1.0	0.98
SGT-38(3)	Rd2	0.031			0.004	0.026	0.006	0.039	0.32	1.1	1.0	
SGT-38(4)	Rd2	0.051	0.008	0.024	0.004		0.005	0.024	0.37	1.3	1.1	0.94
KLN-13(5)	Rd2	0.13	0.017	0.051	0.009	0.047	0.011	0.046	0.25	3.4	0.92	1.3
SGT-10(7)	Rd3	0.054	0.009	0.037	0.006	0.042	0.004	0.081	0.34	1.9	1.0	
SGT-10(8)	Rd3	0.069	0.014	0.028	0.006	0.033	0.006	0.10	0.39	1.8	0.95	1.2
SGT-10(6)	Fd1 core	0.12	0.027	0.077	0.013	0.058	0.009	0.024	0.13	4.7	1.2	1.0
SGT-17(1)	Fd1 core	0.070	0.010	0.032	0.007	0.041	0.006	0.049	1.3	1.8	0.96	0.89
SGT-17(4)	Fd1 core	0.048		0.027	0.006	0.044	0.006	0.027	0.96	1.5	0.94	
KKBS-07(1)	Rd3	0.031	0.007	0.017			0.003	0.055	0.33	1.1	0.69	1.1
KKBS-07(2)	Rd3	0.053	0.012	0.054	0.008		0.007	0.011	0.33	1.1	0.75	

Table 1 (continued)

Sample (test spot)	Type	Dy	Ho	Er	Tm	Yb	Lu	Th	U	∑REE	Ce/Ce*	Eu/Eu*
KKBS-07(3)	Rd3	0.049	0.008	0.044	0.006		0.005	0.068	0.43	0.96	0.81	1.6
YES-09(1)	Fd1	0.11	0.021	0.043	0.012	0.072	0.008	0.008	0.056	3.3	1.4	0.76
YES-09(2)	Fd1	0.18	0.033	0.083	0.019	0.067	0.013	0.008	0.008	2.7	1.8	0.79
YES-13(2)	Fd1	0.15	0.029	0.07	0.009	0.043		0.051	0.16	4.8	1.3	1.3
YES-13(3)	Fd1	0.14	0.031	0.096	0.008	0.091	0.010	0.041	0.008	3.0	1.7	0.97
YES-13(4)	Fd1	0.085	0.019	0.053	0.007	0.040	0.006	0.006	0.004	2.0	1.4	1.2
YES-13(5)	Fd1	0.20	0.037	0.098	0.011	0.083	0.010	0.021	0.041	5.1	1.5	1.1
SGT-10(1)	Fd1	1.2	0.21	0.49	0.065	0.41	0.053	0.007	0.006	29	1.2	0.93
SGT-10(3)	Fd1	0.23	0.039	0.11	0.015	0.094	0.014	0.013	0.018	5.6	1.0	1.1
SGT-10(4)	Fd1	0.33	0.060	0.15	0.017	0.11	0.015	0.011	0.017	8.3	1.1	1.2
SGT-10(5)	Fd1	0.98	0.17	0.40	0.044	0.28	0.050	0.006	0.004	32	1.1	1.1
SGT-13(2)	Fd1	0.16	0.024	0.067	0.009	0.046	0.007	0.021	0.31	4.8	1.3	1.3
SGT-13(5)	Fd1	0.28	0.045	0.10	0.015	0.089	0.014	0.008	0.17	9.8	1.4	1.1
SGT-13(6)	Fd1	0.16	0.026	0.054		0.047	0.008	0.038	0.21	4.1	1.3	1.1
SGT-17(2)	Fd1 rim	0.14	0.026	0.070	0.008	0.057	0.008	0.007	0.007	6.0	1.1	0.94
SGT-17(5)	Fd1 rim	0.19	0.031	0.095	0.013	0.070	0.010	0.007	0.016	5.3	1.3	0.91
SGT-17(6)	Fd1	0.19	0.031	0.077	0.011	0.066	0.008	0.012	0.10	6.1	1.3	0.96
SGT-31(1)	Fd1	0.15	0.026	0.087	0.011	0.079	0.007	0.015	0.006	3.3	1.3	1.2
SGT-31(2)	Fd1	0.51	0.11	0.25	0.022	0.15	0.028	0.007	0.008	15	1.1	0.90
SGT-31(3)	Fd1	0.90	0.18	0.35	0.041	0.19	0.017	0.032	0.72	19	0.94	1.1
SGT-38(5)	Fd1	0.20	0.038	0.068	0.009	0.068	0.008	0.006	0.006	9.3	1.2	1.1
SGT-38(6)	Fd1	0.20	0.033	0.074	0.013	0.066	0.006	0.008	0.008	4.8	1.6	1.1
SGT-38(7)	Fd1	0.58	0.11	0.23	0.030	0.19	0.033	0.008	0.009	13	1.2	1.0
SGT-42(1)	Fd1	0.18	0.030	0.078	0.009	0.048	0.006	0.006	0.006	6.7	1.4	1.2
SGT-42(2)	Fd1	0.30	0.051	0.12	0.013	0.082	0.012	0.007	0.006	11	1.2	1.2
SGT-42(3)	Fd1	0.22	0.039	0.094	0.009	0.065	0.009	0.007	0.006	7.6	1.4	1.1
KGKT-12(1)	Fd2	0.48	0.086	0.19	0.027	0.16	0.012	0.006	0.012	19	0.86	1.6
KGKT-12(3)	Fd2	0.28	0.054	0.12	0.017	0.097	0.011	0.006	0.008	8.9	0.85	1.3
SGT-08(1)	Fd2 core	0.29	0.055	0.13	0.016	0.091	0.011	0.066	0.031	8.3	0.92	2.9
SGT-08(2)	Fd2 rim	0.23	0.043	0.11	0.014	0.069	0.008	0.015	0.017	7.1	0.97	2.6
SGT-13(3)	Fd2	0.32	0.059	0.17	0.019	0.14	0.019	0.007	0.006	11	0.95	2.1
SGT-17(3)	Fd2	0.19	0.032	0.067	0.012	0.078	0.014	0.008	0.008	7.5	0.93	1.8
KLN-13(1)	Fd2	0.42	0.075	0.18	0.023	0.13	0.019	0.009	0.005	24	0.96	1.6
KLN-13(2)	Fd2 rim	0.36	0.067	0.13	0.017	0.12	0.015	0.019	0.006	24	0.92	1.5
KLN-13(3)	Fd2 core	0.27	0.046	0.11	0.011	0.080	0.012	0.009	0.013	14	0.93	1.6

All values are in ppm. Blank indicates below detection limits. Post-Archean Average Shale (PAAS) compositions used for normalizing calculations are from Mclennan (1989). Ce and Eu anomaly values were calculated using $Ce/Ce^{*}=Ce_{SN}/(0.5La_{SN}+0.5Pr_{SN})$ and $Eu/Eu^{*}=Eu_{SN}/(0.67Sm_{SN}+0.33Tb_{SN})$ (Bau et al. 1996)

influence Rd, because they would have resulted in high-Mn dolomites (Jin et al. 2006). Furthermore, moderate-to-high Sr and high Ba contents (Fig. 10b, c) indicate that Rds formed at an early diagenetic stage and only experienced weak recrystallization (Derry 2010; Hecht et al. 1999; Jacobsen and Kaufman 1999; Qing 1998), which is supported by their non-planar-a or planar-s crystal textures and small crystal sizes. Moreover, high Ba contents (Fig. 10c) also imply that these dolomites may have been produced from relatively high-salinity dolomitizing fluids.

From the above, we suggest that the dolomitizing fluids originated from concentrated ancient seawater in the pores under weak oxidizing conditions. Considering the intensely evaporitic environment of the Tarim Basin in the Middle Cambrian, we advocate that formation of the Rds occurred at this time.

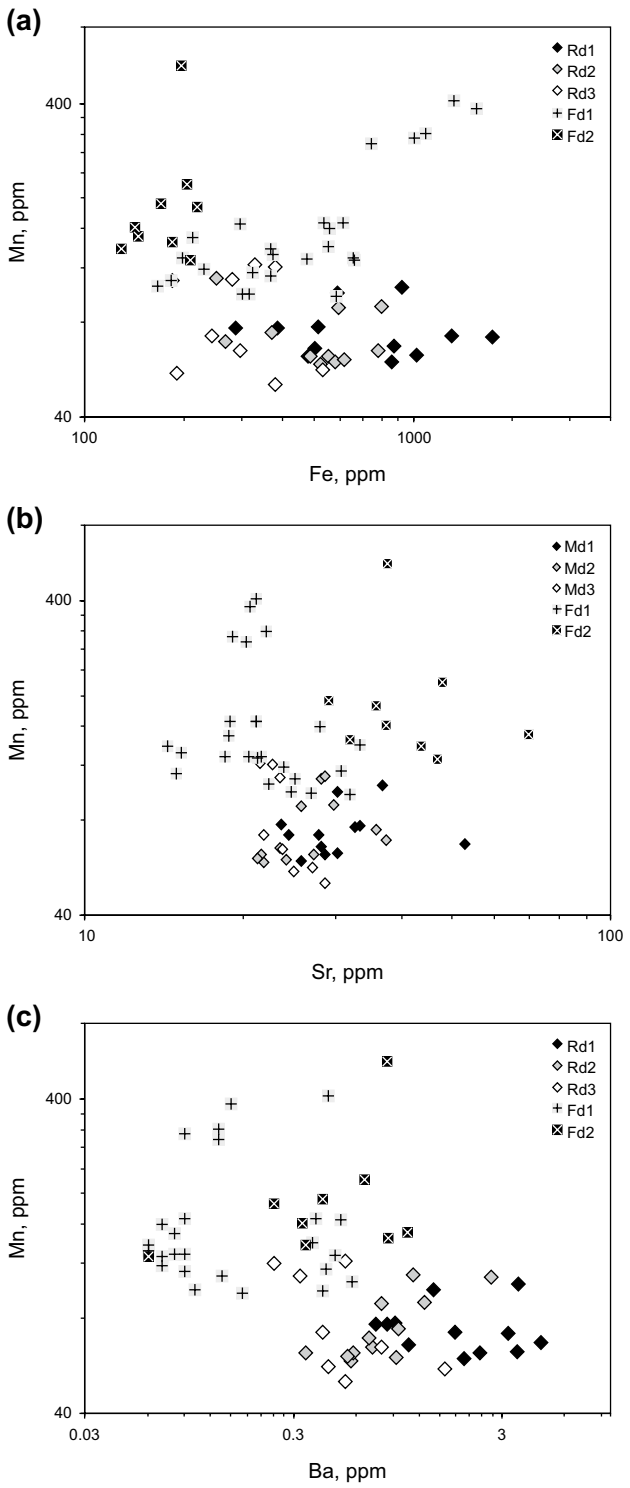

Fig. 10 Cross-plots of **a** Fe, **b** Sr, and **c** Ba versus Mn for different types of dolomites. Detailed data are provided in Table 1

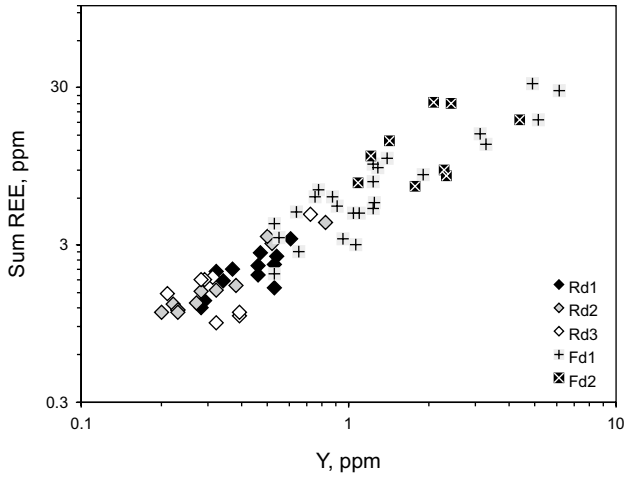

Fig. 11 Cross-plot of Y versus ΣREE for different types of dolomites. Detailed data are provided in Table 1

6.1.2 Origin of Fd1

Fd1 are all distributed in pores and fractures, indicating their direct precipitation from diagenetic fluids rather than replacement of precursor carbonates. Fd1 show planar-e diamond dolomite crystals, suggesting their slow precipitation and sufficient crystallization, which is supported by relatively high Mn, low Ba, and Sr contents (Fig. 10a–c). Moreover, Fd1 show relatively high Mn contents (Fig. 10a–c) and high ΣREE (Fig. 11), suggesting that the diagenetic fluids of Fd1 were hydrothermal fluids.

Fd1 show no Eu anomalies (Table 1); hence, these dolomites probably originated from non-magmatic (crustal) hydrothermal fluids. Note that the Fd1 display roof-shaped REE patterns with significant MREE enrichment and depletion in LREE and HREE (Fig. 12d–f), which are common for hydrothermal carbonates generated by low-pH crustal fluids (Hecht et al. 1999). LREE depletion resulted from the hydrothermal recrystallization of dolomites (Kucera et al. 2009), which is supported by the planar-e diamond dolomite crystals and relatively low Sr contents (Fig. 10b). HREEs are bound to less soluble minerals, which implies HREE depletion in the diagenetic fluids (Bau and Moller 1992; Morgan and Wandless 1980). Additionally, Fd1 show relatively moderate-to-high Fe contents (Fig. 10a), indicating weak oxidation fluid conditions (Azomani et al. 2013), which supports the inference of crustal hydrothermal fluids.

We suggest that the diagenetic fluids of Fd1 were most likely deep-circulating crustal hydrothermal fluids that originated from meteoric or marine water carrying crustal features from detrital rocks. Because Fd1 formed prior to Fd2 in petrography, we infer that the deep-circulating crustal hydrothermal fluids should be earlier than Permian magmatic hydrothermal fluids, and they were controlled by regional tectonic and fault activity. Hence, deep-circulating crustal hydrothermal fluids and Fd1 most likely formed during the Late Caledonian–Early Hercynian, i.e., the Devonian, when

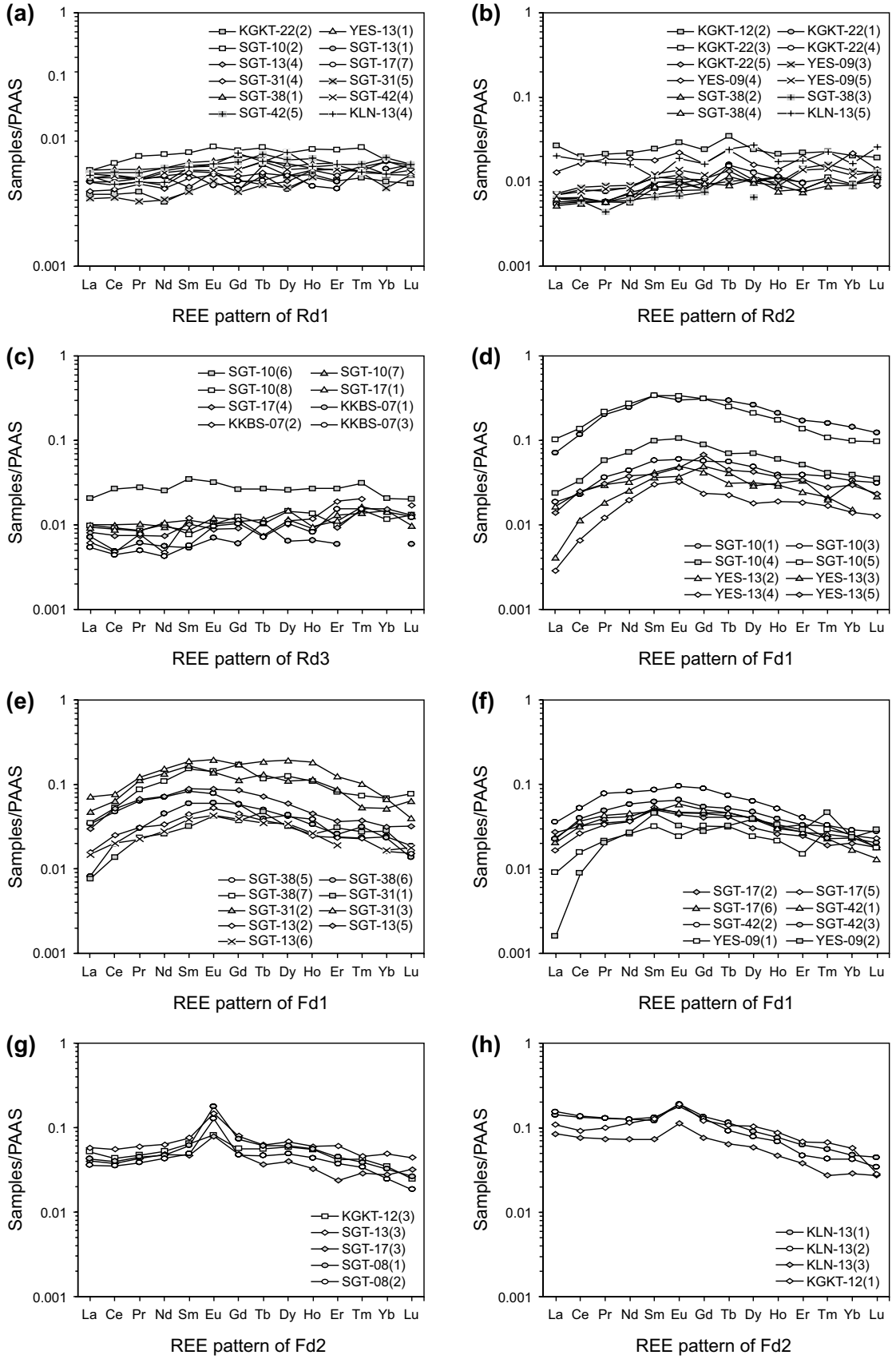

Fig. 12 REE distribution patterns of **a** Rd1, **b** Rd2, **c** Rd3, **d–f** Fd1, and **g–h** Fd2

abundant thrust faults formed in the Tarim Basin (Tang et al. 2012).

6.1.3 Origin of Fd2

Fd2 are all distributed in pores and fractures and show non-planar anhedral crystals with saddle crystal textures and large crystal sizes, suggesting rapid precipitation and insufficient crystallization from diagenetic fluids rather than recrystallization, which is also supported by relatively high Sr contents (Fig. 10b) because recrystallization would result in Sr depletion (Derry 2010; Hecht et al. 1999; Jacobsen and Kaufman 1999; Qing 1998). Moreover, all Fd2 show saddle crystal textures, relatively high Mn contents (Fig. 10a–c), and high ΣREE (Fig. 11), suggesting that the diagenetic fluids of Fd2 should be hydrothermal fluids (Chen et al. 2009a; Huang et al. 2014; Middleton et al. 1993; Sirat et al. 2016). Studies on this kind of pore-filling dolomites showed that the homogenization temperatures could reach 173°–200° (Zhao et al. 2012; Zhu et al. 2010).

Note that the Fd2 display slightly to significantly right-leaning REE patterns with obvious positive Eu anomalies (Fig. 12g, h, Table 1). Positive Eu anomalies may indicate that the hydrothermal fluids should be enriched in Eu^{2+}, indicating an acidic and reducing condition (Frimmel 2009), because the hydrothermal fluids would preferentially provide Eu as Eu^{2+} under acidic conditions (Bau 1991; Kucera et al. 2009; Morgan et al. 2013), and the Eu^{3+} in hydrothermal fluids would be reduced to Eu^{2+} under reducing conditions (Bau et al. 1996; Bau and Moller 1992; Hecht et al. 1999). Reducing conditions are also indicated by relatively low Fe contents (Morford and Emerson 1999) of Fd2 (Fig. 10a).

Based on the acidic, reducing, and extremely high-temperature (~ 200 °C) properties, we infer that hydrothermal fluids were most likely magmatic hydrothermal fluids. The abundant Permian acidic magmatic eruptions and intrusions found in the Tarim Basin (Tian et al. 2010; Yang et al. 2007; Yu et al. 2011; Zhang et al. 2008, 2010, 2014; Zhou et al. 2009) suggest that highly active Permian volcanic–magmatic activities could provide plenty of acidic, reducing, high-temperature, and upward-migrating magmatic hydrothermal fluids enriched in Eu^{2+}. This can also be supported by outcrop evidences (Zhang et al. 2014), integrated isotopic geochemistry (C, O, and Sr), and fluid inclusion microthermometry (Dong et al. 2013). Moreover, plentiful magmatic and siliciclastic rocks (Li et al. 2011a, b; Wang et al. 2010; Zhai 2013) rich in Eu^{2+}-bearing plagioclase developed in the Precambrian basement of the Tarim Basin; therefore, high-temperature hydrothermal fluids migrating upward through the basement can be easily enriched in Eu^{2+} by interacting with these plagioclase-rich rocks and precipitate Fd2 with positive Eu anomalies (Mclennan 1989; Kucera et al. 2009). Therefore, the diagenetic fluids of Fd2 were likely Permian magmatic hydrothermal fluids and the precipitation of Fd2 occurred most probably in the Permian.

6.2 Influence of diagenetic fluids on the formation of diverse reservoir spaces

Three distinct types of diagenetic fluids are interpreted from 5 types of dolomites as described previously; these diagenetic fluids have played an important role in the formation of diverse reservoir spaces. Here, we interpret the influence of different diagenetic fluids on the formation of differing reservoir spaces based on petrography observation.

6.2.1 Influence of dolomitizing fluids related to ancient seawater

Fabric selective dissolution pores were all accompanied by Rds, and no Fds were found in these reservoir spaces (Fig. 8a–d). This observation suggests that deep-circulating crustal hydrothermal fluids and magmatic hydrothermal fluids had no clear influence on the formation of fabric selective dissolution pores. Therefore, the fabric selective dissolution pores may have been altered from primary pores rather than newly generated under the influence of dolomitizing fluids related to ancient seawater (Fig. 6e, f).

Most intraparticle dissolution pores show wave-like irregular boundaries. Furthermore, Rds surrounding the edges of these pores usually display outward-convex crystal morphology (Fig. 8a, b), indicating that no carbonate minerals dissolved during dolomitization. The dolograinstone cements surround the grains in a teeth-like shape (Figs. 7e, 8c, d), suggesting that the interparticle dissolution pores were inherited and altered from primary interparticle pores during dolomitization. Moreover, the bed-parallel dissolution pores are accompanied by enhanced dissolution pores and Fd1 (Fig. 8g), suggesting the occurrence of precursor primary bed-parallel pores because they are expected to provide the necessary channels for diagenetic fluids to generate these pores and precipitate Fd1. Moreover, the intercrystalline dissolution pores are only found in the strongly recrystallized zones (Figs. 7d, 8d, e).

Therefore, we propose that these fabric selective dissolution pores were inherited and altered from precursor primary pores through dolomitization and recrystallization, and the dolomitizing fluids related to ancient seawater rarely generated new reservoir spaces.

6.2.2 Influence of deep-circulating crustal hydrothermal fluids

Fd1 are frequently found growing around the inner walls and take small proportions of fabric non-selective dissolution pores (enhanced dissolution pores) (Fig. 7d–f, h,

i,8f–i). The boundaries of fabric non-selective dissolution pores show outward-convex morphology with regular and smooth profiles, regardless of Fd1 growth around the inner walls (Figs. 7d–e, h, i, 8h, i). Notably, the edges of Rd3 were dissolved as denoted by embayed shapes (Fig. 8e). Therefore, we propose that these fabric non-selective dissolution pores were generated by the dissolution of Rds. The cloudy cores of Fd1 show similar geochemical properties with Rd3 (Fig. 9d, h, Table 1), which indicates that the deep-circulating crustal hydrothermal fluids would have interacted with the Rds.

Based on these arguments, we conclude that the deep-circulating crustal hydrothermal fluids generated the fabric non-selective dissolution pores. These hydrothermal fluids dissolved Rds in the early–middle stages and precipitated Fd1 at a late stage by using Rds as crystallization centers. However, further study is required to interpret the mechanism by which the deep-circulating hydrothermal fluids dissolved Rds.

6.2.3 Influence of magmatic hydrothermal fluids

No Fd2 individually filled the fabric non-selective porosity although they did fill fractures alone, as described before, Fd1 occurred as the first generation of infills of the fabric non-selective dissolution pores, while Fd2 are second-generation infills growing over Fd1. However, Fd1 show straight and smooth crystal edges without any dissolution trails (Fig. 7h, i). Therefore, we infer that magmatic hydrothermal fluids have no dissolution properties and only precipitated Fd2 as the innermost infills, occluding the remaining reservoir spaces that were not occluded by Fd1.

6.3 Porosity evolution controlled by multiple-stage diagenetic fluids

Based on our interpretation of the diagenetic fluids and their influence on the formation of reservoir spaces, this potential sequence of diagenetic fluids can be summarized: (1) dolomitizing fluids related to concentrated ancient seawater in shallow burial environment during the Middle Cambrian; (2) deep-circulating crustal hydrothermal fluids during the Devonian; and (3) magmatic hydrothermal fluids during the Permian.

The average porosity of the samples is 7%–8% (reported by our research before (Li et al. 2015)). More than 260 viewsheds under microscope (> 20 for each sample) were calculated and the volume percent of the Fd1 (2%), Fd2 (1%), fabric selective pores (4%–5%), and fabric non-selective pores (6%) can be measured, so we can propose the porosity evolution of high-quality dolostone reservoir (i.e., dolograinstone reservoir) in the Xiaoerbulak Formation as

Period	After sedimentation before Middle Cambrian	Middle Cambrian	After Middle Cambrian before Devonian	Devonian		After Devonian before Permian	Permian	After Permian
Series of diagenetic fluids	Seawater in pores	Dolomitization fluids derived from residual concentrated basinal seawater	None	Deep-circulating crustal hydrothermal fluids		None	Magmatic hydrothermal fluids	None
The main diagenesis	Compaction cementation	Dolomitization recrystallization	Compaction	Dissolution	Filling	Compaction	Filling	Compaction
Influence on reservoir spaces and porosity	Sharp decrease of primary porosity	Primary pores were altered to dissolution pores Porosity remained unchanged	Slight decrease of porosity	Plentiful dissolution pores and vugs were generated Significant increase of porosity	Dissolution pores and vugs were slightly filled Slight decrease of porosity	Slight decrease of porosity	Dissolution pores and vugs were slightly filled Slight decrease of porosity	Slight decrease of porosity
Porosity evolution of high-quality dolostone reservoirs	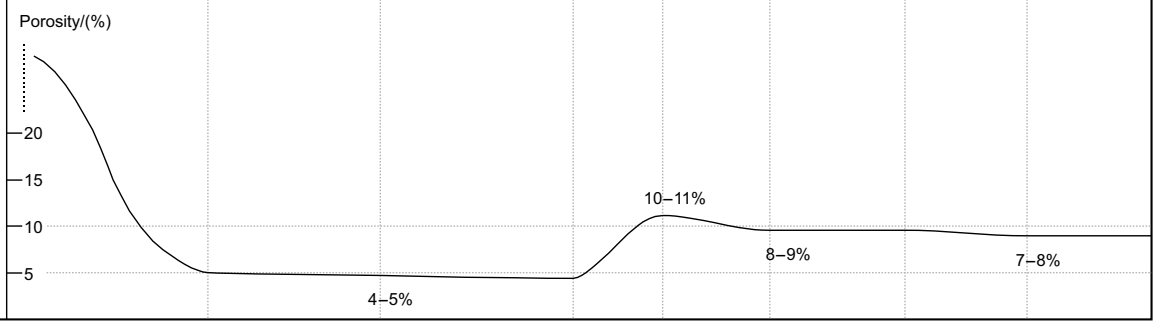							

Fig. 13 The proposed porosity evolution of the high-quality dolostone reservoir controlled by multiple-stage diagenetic fluids in the Lower Cambrian Xiaoerbulak Formation. (The initial porosity is estimated with the dolograinstone regardless of matrix and cements)

follows (Fig. 13): (1) Initial carbonate grains continually precipitated from Early Cambrian seawater and accumulated overlying the seafloor; sediments at this stage were loose and had very high primary porosity (> 20%). (2) Primary sediments were gradually buried, compaction, and cementation strengthened with the increase in burial depth, and the average porosity of newly formed grainstones declined. In the Middle Cambrian, dolomitizing fluids participated in the diagenetic process of grainstones, transformed grainstones into dolograinstone, and altered the interparticle pores to interparticle and intercrystalline dissolution pores, and the average porosity turned to 4%–5% (estimated average porosity from dolograinstone with only fabric selective pores). (3) Deep-circulating crustal hydrothermal fluids participated in the diagenetic process during the Devonian; the fluids dissolved considerable amounts of Rds in the early–middle stages and then precipitated Fd1 in the late stage; the average porosity initially increased to 10%–11% (the porosity of all fabric selective and non-selective pores, regardless of filling minerals in them) and then decreased to 8%–9% (due to filling by Fd1). (4) Magmatic hydrothermal fluids joined in the diagenetic process during the Permian and precipitated Fd2, and the average porosity decreased to 7%–8% (the average porosity of dolograinstone reported by our research before (Li et al. 2015)).

7 Conclusions

Based on the systematically petrographic and in situ geochemical study on different types of dolomites and reservoir spaces in the dolostones of the Lower Cambrian Xiaoerbulak Formation, this research analyzed the types, nature, and origin of the diagenetic fluids of dolomites and their influence on the porosity evolution of this high-quality dolostone reservoir.

Three types of replacive dolomites (Rd) and 2 types of pore-filling dolomites (Fd) are classified based on petrography. And the diagenetic fluids can be divided into three types according to in situ geochemical properties: (1) Rds with slightly left-leaning REE patterns, low ∑REE, low Mn, moderate-to-high Fe and Sr, and high Ba contents were deviated from shallow burial dolomitizing fluids, in an early diagenetic stage, which might probably be related to concentrated ancient seawater in pores; (2) Fd1 with roof-shaped REE patterns, high ∑REE, low Ba and Sr, moderate-to-high Fe, and high Mn contents were likely slowly and sufficiently crystallized from deep-circulating crustal hydrothermal fluids during Devonian; and (3) Fd2 with slightly to significantly right-leaning REE patterns, obvious positive Eu anomaly, high ∑REE, low Fe and Ba, and high Mn and Sr contents were might rapidly and insufficiently precipitated from magmatic hydrothermal fluids during the Permian.

The porosity evolution under the control of multiple-stage diagenetic fluids can be interpreted: (1) Early dolomitizing fluids (concentrated ancient seawater) altered primary pores to fabric selective dissolution pores through dolomitization during the Middle Cambrian; the average porosity was about 4%–5% after compaction, cementation, and dolomitization. (2) During the Devonian, deep-circulating crustal hydrothermal fluids significantly increased porosity in the early stages by dissolving and then slightly decreased the porosity in late stage due to Fd1 precipitation. The average porosity increased to 10%–11% after sufficient dissolution and then slightly decreased to 8%–9% after the Fd1 precipitation. (3) Magmatic hydrothermal fluids only precipitated the Fd2 and slightly decreased the porosity during the Permian. The average porosity slightly decreased to 7%–8%.

Acknowledgements This work is funded by the National Basic Research Program of China (Grant 2012CB214801) and Tarim Oilfield Branch of PetroChina (Grant 041013100042). We thank W. Pan and B. Li for their assistance in field study, Y. Gao for his help in sampling, F. Ma for her guidance in the LA-ICP-MS experiments, and F. Feng, W. Zhang, and X. Jian for their constructive manuscript edits. We also want to present our gratitude to the reviewers and editors for their very detailed and constructive comments.

References

Alibo DS, Nozaki Y. Rare earth elements in seawater: particle association, shalenormalization, and Ce oxidation. Geochim Cosmochim Acta. 1999;63(3–4):363–72. https://doi.org/10.1016/S0016-7037(98)00279-8.

Azomani E, Azmy K, Blamey N, et al. Origin of Lower Ordovician dolomites in eastern Laurentia: controls on porosity and implications from geochemistry. Mar Pet Geol. 2013;40:99–114. https://doi.org/10.1016/j.marpetgeo.2012.10.007.

Bau M. Rare-earth element mobility during hydrothermal and metamorphic fluid-rock interaction and the significance of the oxidation state of europium. Chem Geol. 1991;93(3–4):219–30. https://doi.org/10.1016/0009-2541(91)90115-8.

Bau M, Moller P. Rare earth element fractionation in metamorphogenic hydrothermal calcite, magnesite and siderite. Mineral Petrol. 1992;45(3–4):231–46. https://doi.org/10.1007/BF01163114.

Bau M, Koschinsky A, Dulski P, et al. Comparison of the partitioning behaviours of yttrium, rare earth elements, and titanium between hydrogenetic marine ferromanganese crusts and seawater.

Geochim Cosmochim Acta. 1996;60(10):1709–25. https://doi.org/10.1016/0016-7037(96)00063-4.

Burchfiel BC, Brown ET, Deng Q, et al. Crustal shortening on the margins of the Tien Shan, Xinjiang, China. Int Geol Rev. 1999;41(8):665–700. https://doi.org/10.1080/00206819909465164.

Cai C, Franks SG, Aagaard P. Origin and migration of brines from Paleozoic strata in Central Tarim, China: constraints from Sr-87/Sr-86, delta D, delta O-18 and water chemistry. Appl Geochem. 2001a;16(9–10):1269–84. https://doi.org/10.1016/S0883-2927(01)00006-3.

Cai C, Hu W, Worden RH. Thermochemical sulphate reduction in Cambro-Ordovician carbonates in Central Tarim. Mar Pet Geol. 2001b;18(6):729–41. https://doi.org/10.1016/S0264-8172(01)00028-9.

Cai C, Li K, Li H, et al. Evidence for cross formational hot brine flow from integrated Sr-87/Sr-86, REE and fluid inclusions of the Ordovician veins in Central Tarim, China. Appl Geochem. 2008;23(8):2226–35. https://doi.org/10.1016/j.apgeochem.2008.03.009.

Chen Y, Zhou X, Zhao K, et al. The petrologic rhythm of Lower Ordovician Penglaiba Formation encountered by Well Tazhong 19 and new dolomitization model, Tarim basin. Acta Sedimentol Sin. 2009a;27(2):202–10. https://doi.org/10.14027/j.cnki.cjxb.2009.02.001 **(in Chinese)**.

Chen Y, Zhou X, Yang W. Genesis of Cambrian dolostone and the reservoir evaluation in Tarim Basin. Mar Origin Pet Geol. 2009b;14(4):10–7. https://doi.org/10.3969/j.issn.1672-9854.2009.04.002 **(in Chinese)**.

Chen L, Liu Y, Hu Z, et al. Accurate determinations of fifty-four major and trace elements in carbonate by LA-ICP-MS using normalization strategy of bulk components as 100%. Chem Geol. 2011;284(3–4):283–95. https://doi.org/10.1016/j.chemgeo.2011.03.007.

Choquette PW, Pray LC. Geologic nomenclature and classification of porosity in sedimentary carbonates. Am Asso Pet Geol Bull. 1970;54(2):207–50. https://doi.org/10.1016/0029-8018(69)90006-7.

Derry LA. A burial diagenesis origin for the Ediacaran Shuram-Wonoka carbon isotope anomaly. Earth Planet Sci Lett. 2010;294(1–2):152–62. https://doi.org/10.1016/j.epsl.2010.03.022.

Dong S, Chen D, Qing H, et al. Hydrothermal alteration of dolostones in the Lower Ordovician, Tarim Basin, NW China: multiple constraints from petrology, isotope geochemistry and fluid inclusion microthermometry. Mar Pet Geol. 2013;46:270–86. https://doi.org/10.1016/j.marpetgeo.2013.06.013.

Du J, Pan W. Accumulation conditions and play targets of oil and gas in the Cambrian subsalt dolomite, Tarim Basin, NW China. Pet Explor Dev. 2016;43(3):360–74. https://doi.org/10.1016/S1876-3804(16)30043-X **(in Chinese)**.

Ehrenberg SN, Eberli GP, Keramati M, et al. Porosity-permeability relationships in interlayered limestone-dolostone reservoirs. AAPG Bull. 2006;90(1):91–114. https://doi.org/10.1306/08100505087.

Friedman GM. Identification of carbonate minerals by staining methods. J Sediment Res. 1959;29(1):87–97. https://doi.org/10.1306/74D70894-2B21-11D7-8648000102C1865D.

Frimmel HE. Trace element distribution in Neoproterozoic carbonates as palaeoenvironmental indicator. Chem Geol. 2009;258(3–4):338–53. https://doi.org/10.1016/j.chemgeo.2008.10.033.

Gao S, Liu X, Yuan H, et al. Determination of forty two major and trace elements in USGS and NIST SRM glasses by laser ablation-inductively coupled plasma-mass spectrometry. Geostand Geoanal Res. 2002;26(2):181–96. https://doi.org/10.1111/j.1751-908X.2002.tb00886.x.

Gregg JM, Sibley DF. Epigenetic dolomization and the origin of xenotopic dolomite texture. J Sediment Res. 1984;54(3):908–31. https://doi.org/10.1306/212F8535-2B24-11D7-8648000102C1865D.

Gu J, Jia J, Fang H. Reservoir characteristics and genesis of high-porosity and high-permeability reservoirs in Tarim Basin. Chin Sci Bull. 2002;47(S):12–9. https://doi.org/10.1007/bf02902813.

Hardie LA. Dolomitization: a critical view of some current views. J Sediment Petrol. 1987;57(1):166–83. https://doi.org/10.1306/212F8AD5-2B24-11D7-8648000102C1865D.

Hecht L, Freiberger R, Gilg HA, et al. Rare earth element and isotope (C, O, Sr) characteristics of hydrothermal carbonates: genetic implications for dolomite-hosted talc mineralization at Göpfersgrün (Fichtelgebirge, Germany). Chem Geol. 1999;155(1–2):115–30. https://doi.org/10.1016/S0009-2541(98)00144-2.

Huang W, Wang A, Wan H, et al. Discussion on characteristics of the Cambrian-Ordovician carbonate rocks reservoirs and origin of dolostones in Tarim Basin. J Palaeogeogr. 2012;14(2):197–208. https://doi.org/10.1007/s11783-011-0280-z **(in Chinese)**.

Huang S, Huang K, Lu J, et al. The relationship between dolomite textures and their formation temperature: a case study from the Permian-Triassic of the Sichuan Basin and the Lower Paleozoic of the Tarim Basin. Pet Sci. 2014;11(1):39–51. https://doi.org/10.1007/s12182-014-0316-7.

Jacobsen SB, Kaufman AJ. The Sr, C and O isotopic evolution of Neoproterozoic seawater. Chem Geol. 1999;161(1–3):37–57. https://doi.org/10.1016/S0009-2541(99)00080-7.

Ji C, Qing H, Chen D, et al. Characteristics and dolomitization of Upper Cambrian to Lower Ordovician dolomite from outcrop in Keping Uplift, Western Tarim Basin, Northwest China. Acta Geologica Sinica-English Edition. 2013;87(4):1005–18. https://doi.org/10.1111/1755-6724.12106.

Jin Z, Zhu D, Hu W, et al. Geological and geochemical signatures of hydrothermal activity and their influence on carbonate reservoir beds in the Tarim basin. Acta Geol Sin. 2006;80(2):245–53. https://doi.org/10.3321/j.issn:0001-5717.2006.02.009 **(in Chinese)**.

Jochum KP, Scholz D, Stoll B, et al. Accurate trace element analysis of speleothems and biogenic calcium carbonates by LA-ICP-MS. Chem Geol. 2012;318–319:31–44. https://doi.org/10.1016/j.chemgeo.2012.05.009.

Kamber BS, Webb GE. Transition metal abundances in microbial carbonate: a pilot study based on in situ LA-ICP-MS analysis. Geobiology. 2007;5(4):375–89. https://doi.org/10.1111/j.1472-4669.2007.00129.x.

Kirmaci MZ, Akdag K. Origin of dolomite in the Late Cretaceous-Paleocene limestone turbidites, Eastern Pontides, Turkey. Sediment Geol. 2005;181(1–2):39–57. https://doi.org/10.1016/j.sedgeo.2005.07.003.

Kucera J, Cempirek J, Dolnicek Z, et al. Rare earth elements and yttrium geochemistry of dolomite from post-Variscan vein-type mineralization of the Nizky Jesenik and Upper Silesian Basins, Czech Republic. J Geochem Explor. 2009;103(2–3):69–79. https://doi.org/10.1016/j.gexplo.2009.08.001.

Lazartigues AV, Sirois P, Savard D. LA-ICP-MS analysis of small samples: carbonate reference materials and larval fish otoliths. Geostand Geoanal Res. 2014;38(2):225–40. https://doi.org/10.1111/j.1751-908X.2013.00248.x.

Li D. Hydrocarbon occurrences in the petroliferous basins of western China. Mar Pet Geol. 1995;12(1):26–34. https://doi.org/10.1016/0264-8172(95)90385-W.

Li K, Cai C, He H, et al. Origin of palaeo-waters in the Ordovician carbonates in Tahe oilfield, Tarim Basin: constraints from fluid inclusions and Sr, C and O isotopes. Geofluids. 2011a;11(1):71–86. https://doi.org/10.1111/j.1468-8123.2010.00312.x.

Li Q, Hu W, Qian Y, et al. Features of dissolved dolostone reservoirs in the Xiaoerbulak Formation, Tarim Basin. Oil Gas Geol.

2011b;32(4):522–30. https://doi.org/10.11743/ogg20110405 **(in Chinese)**.

Li X, Mo X, Yu X, et al. Petrology and geochemistry of the early Mesozoic pyroxene andesites in the Maixiu Area, West Qinling, China: products of subduction or syn-collision? Lithos. 2013;172:158–74. https://doi.org/10.1016/j.lithos.2013.04.010.

Li B, Deng S, Chen Y, et al. The reservoir modeling of platform margin dolostone of Xiaoerblak Formation, lower Cambrian, Kalpin Area, Tarim Basin. Nat Gas Geosci. 2015;26(7):1233–44. https://doi.org/10.11764/j.issn.1672-1926.2015.07.1233 **(in Chinese)**.

Li Q, Jiang Z, Hu W, et al. Origin of dolomites in the Lower Cambrian Xiaoerbulak Formation in the Tarim Basin, NW China: implications for porosity development. J Asian Earth Sci. 2016;115:557–70. https://doi.org/10.1016/j.jseaes.2015.10.022.

Liu X, Jin Z, Bai G, et al. Formation and distribution characteristics of Proterozoic-Lower Paleozoic marine giant oil and gas fields worldwide. Pet Sci. 2017;14(2):237–60. https://doi.org/10.1007/s12182-017-0154-5.

Machel HG. Concepts and models of dolomitization: a critical appraisal. In: Braithwaite CJR, Rizzi G, Darke G, editors. The geometry and petrogenesis of dolomite hydrocarbon reservoirs. London: Geological Society; 2004. p. 7–63. https://doi.org/10.1144/GSL.SP.2004.235.01.02.

McLennan SM. Rare earth elements in sedimentary rocks: influence of provenance and sedimentary processes. Geochem Mineral Rare Earth Elem. 1989. https://doi.org/10.1515/9781501509032-010.

Middleton K, Coniglio M, Sherlock R, et al. Dolomitization of Middle Ordovician carbonate reservoirs, southwestern Ontario. Bull Can Pet Geol. 1993;41(2):150–63. https://doi.org/10.1016/0307-904X(93)90057-N.

Morford JL, Emerson S. The geochemistry of redox sensitive trace metals in sediments. Geochim Cosmochim Acta. 1999;63(11–12):1735–50. https://doi.org/10.1016/S0016-7037(99)00126-X.

Morgan JW, Wandless GA. Rare earth elements in some hydrothermal minerals-Evidence of crystallographic control. Geochim Cosmochim Acta. 1980;44(7):973–80. https://doi.org/10.1016/0016-7037(80)90286-0.

Morgan R, Orberger B, Rosiere CA, et al. The origin of coexisting carbonates in banded iron formations: a micro-mineralogical study of the 2.4 Ga Itabira Group, Brazil. Precambr Res. 2013;224:491–511. https://doi.org/10.1016/j.precamres.2012.10.013.

Morrow DW. Regional subsurface dolomitization: models and constraints. Geosci Can. 1998;25(2):57–70.

Ni X, Shen A, Chen Y, et al. Cambrian carbonate plateform types, plateform margin segmentation characteristics and exploration enlightenment in Tarim Basin. Nat Gas Geosci. 2015;26(7):1245–55. https://doi.org/10.11764/j.issn.1672-1926.2015.07.1245 **(in Chinese)**.

Pan W, Liu Y, Dickson J, et al. The geological model of hydrothermal activity in outcrop and the characteristics of carbonate hydrothermal karst of Lower Paleozoic in Tarim basin [in Chinese with English abstract]. Acta Sedimentol Sin. 2009;27(5):983–94. https://doi.org/10.14027/j.cnki.cjxb.2009.05.023.

Pan W, Hu X, Liu Y, et al. Geological and geochemical evidences for two sources of hydrothermal fluids found in Ordovican carbonate rocks in northwestern Tarim Basin. Acta Pet Sin. 2012;28(8):2515–24. https://doi.org/10.1007/s11783-011-0280-z **(in Chinese)**.

Pu R, Dang X, Xu J, et al. Permian division and correlation and distribution of volcanic rocks of Tarim Basin. Acta Pet Sin. 2011;27(1):166–80. https://doi.org/10.1007/s11769-011-0445-5 **(in Chinese)**.

Qian Y, You D, Chen D, et al. The petrographic and geochemical signatures and implication of origin of the Middle and Upper Cambrian dolostone in eastern margin Tarim: comparative studies with the Whirlpool point of the Western Canada Sedimentary Basin. Acta Pet Sin. 2012;28(8):2525–41. https://doi.org/10.1007/s11783-011-0280-z **(in Chinese)**.

Qing H. Petrography and geochemistry of early-stage, fine- and medium-crystalline dolomites in the Middle Devonian Presqu'ile Barrier at Pine Point, Canada. Sedimentology. 1998;45(2):433–46. https://doi.org/10.1046/j.1365-3091.1998.0154f.x.

Shen A, Zheng J, Chen Y, et al. Characteristics, origin and distribution of dolomite reservoirs in Lower-Middle Cambrian, Tarim Basin, NW China. Pet Explor Dev. 2016;43(3):375–85. https://doi.org/10.1016/S1876-3804(16)30044-1.

Sibley DF, Gregg JM. Classification of dolomite rock textures. J Sediment Petrol. 1987;57(6):967–75. https://doi.org/10.1306/212f8cba-2b24-11d7-8648000102c1865d.

Sirat M, Al-Aasm IS, Morad S, et al. Saddle dolomite and calcite cements as records of fluid flow during basin evolution: paleogene carbonates, United Arab Emirates. Mar Pet Geol. 2016;74:71–91. https://doi.org/10.1016/j.marpetgeo.2015.11.005.

Song J, Luo P, Yang S, et al. Reservoirs of Lower Cambrian microbial carbonates, Tarim Basin, NW China. Petrol Explor Dev. 2014;41(4):449–59. https://doi.org/10.1016/S1876-3804(14)60051-3.

Sonnenberg SA, Pramudito A. Petroleum geology of the giant Elm Coulee field, Williston Basin. AAPG Bull. 2009;93(9):1127–53. https://doi.org/10.1306/05280909006.

Sun S. Dolomite reservoirs: porosity evolution and reservoir characteristics. AAPG Bull. 1995;79(2):186–204. https://doi.org/10.1306/8D2B14EE-171E-11D7-8645000102C1865D.

Tang L. Major evolutionary stages of Tarim Basin in Phanerozoic Time. Earth Sci Front. 1997;4(3–4):318–24 **(in Chinese)**.

Tang L, Qi L, Qiu H, et al. Poly-phase differential fault movement and hydrocarbon accumulation of the Tarim Basin, NW China. Acta Pet Sin. 2012;28(8):2569–83. https://doi.org/10.1016/j.sedgeo.2012.06.004 **(in Chinese)**.

Tian W, Campbell IH, Allen CM, et al. The Tarim picrite-basalt-rhyolite suite, a Permian flood basalt from northwest China with contrasting rhyolites produced by fractional crystallization and anatexis. Contrib Miner Petrol. 2010;160(3):407–25. https://doi.org/10.1007/s00410-009-0485-3.

Wang Q, Nishidai T, Coward MP. The Tarim Basin, NW China: formation and aspects of petroleum geology. J Pet Geol. 1992;15(1):5–34. https://doi.org/10.1111/j.1747-5457.1992.tb00863.x.

Wang X, Jin Z, Hu W, et al. Using in situ REE analysis to study the origin and diagenesis of dolomite of Lower Paleozoic, Tarim Basin. Sci China Ser D Earth Sci. 2009;52(5):681–93. https://doi.org/10.1007/s11430-009-0057-4.

Wang F, Wang B, Shu L. Continental tholeiitic basalt of the Akesu area (NW China) and its implication for the Neoproterozoic rifting in the northern Tarim. Acta Pet Sin. 2010;26(2):547–58 **(in Chinese)**.

Warren J. Dolomite: occurrence, evolution and economically important associations. Earth Sci Rev. 2000;52(1–3):1–81. https://doi.org/10.1016/S0012-8252(00)00022-2.

Yang S, Li Z, Chen H, et al. Permian bimodal dyke of Tarim Basin, NW China: geochemical characteristics and tectonic implications. Gondwana Res. 2007;12(1–2):113–20. https://doi.org/10.1016/j.gr.2006.10.018.

You X, Lin C, Zhu J, et al. Primary microbial dolomite precipitation in culture experiments and in stromatolite formations: implications for the dolomite problem. Carpathian J Earth Environ Sci. 2015;10(3):197–206.

Yu X, Yang S, Chen H, et al. Permian flood basalts from the Tarim Basin, Northwest China: SHRIMP zircon U-Pb dating and geochemical characteristics. Gondwana Res. 2011;20(2–3):485–97. https://doi.org/10.1016/j.gr.2010.11.009.

Zhai M. The main old lands in China and assembly of Chinese unified continent. Sci China Ser D Earth Sci. 2013;56(11):1829–52. https://doi.org/10.1007/s11430-013-4665-7.

Zhang C, Li X, Li Z, et al. A Permian layered intrusive complex in the western Tarim block, northwestern China: product of a Ca. 275 Ma mantle plume. J Geol. 2008;116(3):269–87. https://doi.org/10.1086/587726.

Zhang J, Hu W, Qian Y, et al. Formation of saddle dolomites in Upper Cambrian carbonates, western Tarim Basin (northwest China): implications for fault-related fluid flow. Mar Pet Geol. 2009;26(8):1428–40. https://doi.org/10.1016/j.marpetgeo.2009.04.004.

Zhang C, Xu Y, Li Z, et al. Diverse Permian magmatism in the Tarim Block, NW China: genetically linked to the Permian Tarim mantle plume? Lithos. 2010;119(3–4):537–52. https://doi.org/10.1016/j.lithos.2010.08.007.

Zhang J, Hu W, Wang X, et al. Character and origin of Cambrian hydrothermal dolomite conglomeration in the northwestern margin of Tarim Basin. Acta Geol Sin. 2011;85(2):234–45. https://doi.org/10.3724/SP.J.1011.2011.00181 **(in Chinese)**.

Zhang W, Guan P, Jian X, et al. In situ geochemistry of Lower Paleozoic dolomites in north-western Tarim basin: implications for the nature, origin and evolution of diagenetic fluids. Geochem Geophys Geosyst. 2014;15(7):2744–64. https://doi.org/10.1002/2013GC005194.

Zhao H, Jones B. Distribution and interpretation of rare earth elements and yttrium in Cenozoic dolostones and limestones on Cayman Brac, British West Indies. Sediment Geol. 2013;284:26–38. https://doi.org/10.1016/j.sedgeo.2012.10.009.

Zhao W, Luo P, Chen G, et al. Origin and reservoir rock characteristics of dolostones in the Early Triassic Feixianguan Formation, NE Sichuan Basin, China: significance for future gas exploration. J Pet Geol. 2005;28(1):83–100. https://doi.org/10.1111/j.1747-5457.2005.tb00072.x.

Zhao C, Yu B, Zhang C, et al. A discussion on the formation mechanism of dolomite associated with hydrothermal solution in Tazhong area. Acta Petrologica et Mineralogica. 2012;31(2):164–72. https://doi.org/10.1007/s11783-011-0280-z **(in Chinese)**.

Zheng H, Wu M, Wu X, et al. Oil-gas exploration prospect of dolomite reservoir in the Lower Paleozoic of Tarim Basin. Acta Pet Sin. 2007;28(2):1–8. https://doi.org/10.3321/j.issn:0253-2697.2007.02.001 **(in Chinese)**.

Zhou M, Zhao J, Jiang C, et al. OIB-like, heterogeneous mantle sources of Permian basaltic magmatism in the western Tarim Basin, NW China: implications for a possible Permian large igneous province. Lithos. 2009;113(3–4):583–94. https://doi.org/10.1016/j.lithos.2009.06.027.

Zhu D, Jin Z, Hu W. Hydrothermal recrystallization of the Lower Ordovician dolomite and its significance to reservoir in northern Tarim Basin. Sci China Ser D Earth Sci. 2010;53(3):368–81. https://doi.org/10.1007/s11430-010-0028-9.

Zhu D, Meng Q, Jin Z, et al. Formation mechanism of deep Cambrian dolomite reservoirs in the Tarim Basin, northwestern China. Mar Pet Geol. 2014; 59:232–44. https://doi.org/10.1016/j.marpetgeo.2014.08.022.